



1 An Aerosol Climatology via Remote Sensing over Metro Manila, Philippines

2

3 Genevieve Rose Lorenzo^{1,2}, Avelino F. Arellano¹, Maria Obiminda Cambaliza^{2,3}, Christopher
4 Castro¹, Melliza Templonuevo Cruz^{2,4}, Larry Di Girolamo⁵, Glenn Franco Gacal², Miguel
5 Ricardo A. Hilario¹, Nofel Lagrosas⁶, Hans Jarett Ong², James Bernard Simpas^{2,3}, Sherdon Niño
6 Uy², and Armin Sorooshian^{1,7}

7

8 ¹Department of Hydrology and Atmospheric Sciences, University of Arizona, Tucson, Arizona,
9 85721, USA

10 ²Air Quality Dynamics-Instrumentation & Technology Development Laboratory, Manila
11 Observatory, Quezon City, 1108, Philippines

12 ³Department of Physics, School of Science and Engineering, Ateneo de Manila University,
13 Quezon City, 1108, Philippines

14 ⁴Institute of Environmental Science and Meteorology, University of the Philippines, Diliman,
15 Quezon City, 1101, Philippines

16 ⁵Department of Atmospheric Science, University of Illinois, Urbana-Champaign, Illinois, 61801,
17 USA

18 ⁶Center for Environmental Remote Sensing, Chiba University, Chiba, 263-8522, Japan

19 ⁷Department of Chemical and Environmental Engineering, University of Arizona, Tucson,
20 Arizona, 85721, USA

21

22 *Correspondence to:* armin@arizona.edu



23 **Abstract**

24 Aerosol particles in Southeast Asia have a complex life cycle and consequently are challenging
25 to characterize. The diverse topography and weather in the region complicate the situation. An
26 aerosol climatology was established based on AERONET data (December 2009 to October
27 2018) for clear sky days in Metro Manila, Philippines. Aerosol optical depth (AOD) values were
28 highest in August, coinciding with the summer southwest monsoon, due partly to fine particles
29 from urban aerosol particles, including soot. Also, August corresponds to the burning season in
30 Insular Southeast Asia when smoke is often transported to Metro Manila. Clustering of
31 AERONET volume size distributions (VSD) resulted in five aerosol particle sources based on
32 the position and magnitude of their peaks in the VSD and the contributions of specific particle
33 species to AOD per cluster based on MERRA-2. The clustering showed that the majority of
34 aerosol particles above Metro Manila were from a clean marine source (58%), which could be
35 related to AOD values there being relatively smaller than in other cities in the region. The
36 following are the other particle sources over Metro Manila: fine polluted (20%), mixed polluted
37 (12%), urban/industrial (5%), and cloud processing (5%). Furthermore, MERRA-2 AOD data
38 over Southeast Asia were analyzed using empirical orthogonal functions. Along with AOD
39 fractional compositional contributions and wind regimes, four dominant aerosol particle air
40 masses emerged: two sulfate air masses from East Asia, an organic carbon source from
41 Indonesia, and a sulfate source from the Philippines. Knowing the local and regional aerosol
42 particle air masses that impact Metro Manila is useful in identifying the sources while gaining
43 insight on how aerosol particles are affected by long-range transport and their impact on regional
44 weather.



45 **1. Introduction**

46 Although Southeast Asia is one of the most rapidly developing regions in the world, there have
47 been limited studies characterizing aerosol particles in the area (Tsay et al., 2013; Lee et al.,
48 2018; Chen et al., 2020). The region represents a complex geographic, meteorological, and
49 hydrological environment making it challenging to understand aerosol particle characteristics,
50 especially interactions between aerosol particles with their environment (Reid et al., 2013). The
51 island of Luzon in the Philippines in particular is very populated and is characterized by high
52 levels of anthropogenic emissions superimposed on natural emissions from the surrounding
53 waters (AzadiAghdam et al., 2019) and long-range transport of emissions from areas such as
54 Indonesia and East Asia (Braun et al., 2020; Hilario et al., 2020a; Hilario et al., 2020b; Hilario et
55 al., 2021a). The presence of clouds in the area (Hong and Di Girolamo, 2020) makes space-borne
56 remote sensing of aerosol particles very challenging (Reid et al., 2013; Lin et al., 2014). These
57 reasons motivated the NASA Cloud, Aerosol, and Monsoon Processes Philippines Experiment
58 (CAMP²Ex) airborne measurement campaign in 2019 to understand the interaction between
59 tropical meteorology and aerosol particles (Di Girolamo et al., 2015; Reid et al., 2023). Prior to
60 the airborne measurements, intensive surface-based measurements were conducted as part of the
61 CAMP²Ex weatHER and CompoSition Monitoring (CHECSM) study between July 2018 and
62 October 2019.

63 Aerosol climatology studies in different regions have proved beneficial to understand temporal
64 characteristics of aerosol particle concentrations and properties, in addition to identifying
65 potential source regions along with interactions with clouds and rainfall (Stevens and Feingold,
66 2009; Li et al., 2011; Tao et al., 2012; Crosbie et al., 2014; Kumar et al., 2015; Alizadeh-
67 Choobari and Gharaylou, 2017; Mora et al., 2017; Aldhaif et al., 2021). The NASA AErosol
68 RObotic NETwork (AERONET) (Holben et al., 1998) is pivotal in providing broad temporal
69 coverage in specific locations with a column-based perspective from the ground up. To our
70 knowledge, there has not been a remote sensing-based aerosol climatology study for the Metro
71 Manila region of Luzon, which has approximately 16 cities, a population of 12.88 million, and a
72 high population density of 20,800 km⁻² (PSA, 2016; Alas et al., 2018). Studying this area is
73 informative owing to the wide dynamic range in aerosol particle and weather conditions, which
74 are interconnected. Aerosol particle lifecycle in the region is impacted by Philippine weather that
75 is marked by two distinct monsoons, typhoons, and impacts from El Niño-Southern Oscillation
76 and Madden-Julian Oscillation (Cruz et al., 2013; Xian et al., 2013; Reid et al., 2012; Reid et al.,
77 2015; Hilario et al., 2021b).

78 Regional analysis of aerosol particles in Southeast Asia and Asia in general show the prevalence
79 of biomass burning in the region, as well as the larger influence of anthropogenic emissions in
80 East Asia (Nakata et al., 2018). These large prevalent sources may overshadow other relevant but
81 weaker sources in the region, such as local sources. Due to the complex nature of aerosol
82 particles, analysis techniques such as principal component analysis and clustering along with
83 recent improvements in gridded datasets help detect spatial and temporal patterns that would
84 otherwise be difficult to make with noise interference and even weak signals (Li et al., 2013;
85 Sullivan et al., 2017; Plymale et al., 2021). Understanding the dominant air masses around
86 Southeast Asia will help in distinguishing local and transported particles that influence the
87 aerosol climatology in Metro Manila.



88 The goal of this study is to use multi-year AERONET data along with other complementary
 89 datasets to address the following questions: (1) what are the monthly characteristics of aerosol
 90 particles over Metro Manila, Philippines?; (2) what are the possible sources and factors
 91 influencing the observed characteristics?; (3) what relationships are evident between aerosol
 92 particles and cloud characteristics?; and (4) what are the regional and local aerosol particle air
 93 masses that influence Metro Manila?
 94

95 **2. Methods**

96 This work relies on analysis of several datasets summarized in Table 1 and the following
 97 subsections. The common time range used for all datasets is between January 2009 and October
 98 2018.

99 **Table 1:** Summary of datasets over Metro Manila used in this work covering the period from
 100 January 2009 to October 2018.

Parameter	Data Source	Spatial Coverage	Data Repository
Aerosol Optical Depth (500 nm)	AERONET	14.635°N, 121.078°E	(AERONET) https://aeronet.gsfc.nasa.gov
Asymmetry Factor (440 nm - 1020 nm)	AERONET	14.635°N, 121.078°E	
Extinction Angstrom Exponent (440 nm - 870 nm)	AERONET	14.635°N, 121.078°E	
Fine Mode Fraction	AERONET	14.635°N, 121.078°E	
Precipitable Water	AERONET	14.635°N, 121.078°E	
Single Scattering Albedo (440 nm - 1020 nm)	AERONET	14.635°N, 121.078°E	
Refractive Index (Real and Imaginary; 440 nm - 1020 nm)	AERONET	14.635°N, 121.078°E	
Volume Size Distribution	AERONET	14.635°N, 121.078°E	
Low Cloud Fraction (MODIS)	MERRA-2	14.25°N - 14.75°N, 120.9375°E - 121.5625°E	(MERRA-2) https://disc.gsfc.nasa.gov/
Planetary Boundary Layer Height	MERRA-2	14.25°N - 14.75°N, 120.9375°E - 121.5625°E	
Relative Humidity (975 mb)	MERRA-2	14.25°N - 14.75°N, 120.9375°E - 121.5625°E	
Sea Level Pressure	MERRA-2	14.25°N - 14.75°N, 120.9375°E - 121.5625°E	
Temperature (975 mb)	MERRA-2	14.25°N - 14.75°N, 120.9375°E - 121.5625°E	
Wind (975 mb)	MERRA-2	14.25°N - 14.75°N, 120.9375°E - 121.5625°E	
Precipitation	PERSIANN	14.5°N - 15.0°N, 120.75°E - 121.25°E	(PERSIANN) https://chrdata.eng.uci.edu/

101



102 **2.1 Datasets**

103 2.1.1 AERONET

104 The central dataset used is that of sun photometer measurements and derived (inversion)
105 parameters from the AERONET (Holben et al., 1998) site at the Manila Observatory in Quezon
106 City, Philippines (14.64° N, 121.08° E, ~70 m. a. s. l.). Direct sunlight extinction measurements
107 were made at nominal wavelengths of 340, 380, 440, 500, 675, 870, 940, and 1020 nm, from
108 which aerosol optical depth (AOD) was calculated (except for 940 nm, which is for water vapor)
109 (Eck et al., 2013). AOD is a commonly used proxy for aerosol particle loading in the air column
110 from the ground up (Holben et al., 2001); higher AOD translates to more aerosol particle
111 extinction in the column above a location. The extinction angstrom exponent (EAE) and the fine
112 mode fraction (FMF) are also AERONET direct sun products that are retrieved after the
113 application of a spectral de-convolution algorithm (O'Neill et al., 2003). For the inversion
114 products, it is through radiative retrievals that the volume size distribution (VSD) and complex
115 refractive index (RI) are gathered (Schuster et al., 2005) and from which single scattering albedo
116 (SSA) and asymmetry factor (AF) are calculated.

117 For the inversions, four wavelengths (440, 670, 870, and 1020 nm) of the radiometer spectral
118 channels were chosen for diffuse radiance measurements and to avoid gas absorption (Dubovik
119 et al., 1998). Version 3 Direct Sun and Inversion algorithms (AERONET, 2019; Giles et al.,
120 2019) were used with the Almuqantar Sky Scan Scenario to derive the following parameters with
121 level 2.0 (automatically cloud-cleared and quality controlled datasets with pre- and post-field
122 calibrations) data quality: column AOD (500 nm), fine mode fraction (500 nm), extinction
123 angstrom exponent (440 – 870 nm), precipitable water (940 nm), SSA (440, 670, 870, and 1020
124 nm), asymmetry factor (440, 670, 870, and 1020 nm), refractive index (440, 670, 870, and 1020
125 nm), and VSD. The version 3 products are able to keep fine mode aerosol particle data (haze and
126 smoke) as well as remove optically thin cirrus clouds in order to retain more aerosol particle
127 measurements in the database (Giles et al., 2019). Cloud screening in the version 3 product
128 improves remote sensing measurements in Southeast Asia in general, where cirrus clouds are
129 pervasive (Reid et al., 2013). At most, a total of 29,037 direct sun and 1419 inversion
130 AERONET daytime data points were available between January 2009 and October 2018.

131 2.1.2 MERRA-2

132 Modern Era-Retrospective Analysis for Research and Applications, Version 2 (MERRA-2: 0.5°
133 × 0.625° approximate resolution) meteorological and aerosol particle composition data
134 (Bosilovich, 2016; Gelaro et al., 2017; Randles et al., 2017) were acquired for the area around
135 Manila Observatory (14.25°N – 14.75°N, 120.9375°E – 121.5625°E). The following products
136 were used: M2I3NPASM Assimilated Meteorological Fields (3-hourly) for 975 mb level winds,
137 temperature, relative humidity, and sea level pressure; M2T1NXFLX Surface Flux Diagnostics
138 (1-hourly from 00:30 UTC time-averaged) 2D for planetary boundary layer height; and
139 M2T1NXCSP COSP Satellite Simulator (1-hourly from 00:30 UTC time-averaged) for MODIS
140 mean low cloud fraction (cloud top pressure > 680 hPa).

141 MERRA-2 meteorological and aerosol particle composition monthly data (Bosilovich, 2016;
142 Gelaro et al., 2017; Randles et al., 2017) were also acquired for a larger region, the Southeast
143 Asia region (0° - 30°N, 105°E – 135°E) for the period from 2009 to 2018. This is within the
144 spatial domain of the CAMP²Ex airborne measurement campaign which, as mentioned earlier,
145 targets the interaction between tropical meteorology and aerosol particles. The following datasets



146 (0.5° latitude and 0.625° longitude resolution) were used: MERRA-2 `tavgM_2d_aer_Nx`:
147 Aerosol Assimilation (M2TMNXAER) for Total AOD and speciated AOD (Sulfate, Black
148 Carbon (BC), Organic Carbon (OC), Dust, and Sea Salt) and MERRA-2 `instM_3d_ana_Np`:
149 Analyzed Meteorological Fields (M2IMNPANA) for 1000 hPa and 725 hPa level U and V
150 winds. The monthly meteorological and aerosol particle composition data for the region will be
151 used for empirical orthogonal functions, which will be described later.

152 2.1.3 MISR

153 Monthly AOD data (Level 3 Global Aerosol: 0.5° × 0.5° spatial resolution) from 2009 to 2018
154 are used from the Multi-angle Imaging SpectroRadiometer (MISR), (Diner et al., 2007; Garay et
155 al., 2018). Level 3 products are global maps of parameters available in Level 2 (measurements
156 derived from the instrument data) products. MISR has relatively more accurate AOD and agrees
157 better with AERONET data compared to other satellite products due to its multi-angle
158 measurements (Choi et al., 2019; Kuttippurath and Raj, 2021). Monthly median AOD (bin 0)
159 were extracted for Southeast Asia (0.25° - 30.25°N, 104.75°E – 134.75°E) within the CAMP²Ex
160 region. They are used for comparison to the AERONET (over Metro Manila) and MERRA-2
161 (Southeast Asia) monthly AOD values.

162 2.1.4 PERSIANN

163 Hourly precipitation data were obtained from the Precipitation Estimation from the Remotely
164 Sensed Information using Artificial Neural Networks (PERSIANN) (Nguyen et al., 2019)
165 database of the Center for Hydrometeorology and Remote Sensing (CHRS) at the University of
166 California, Irvine (UCI). Hourly data were accumulated for running three-day totals, which were
167 compared to AERONET data. The data were averaged between the four grids that included the
168 area of interest as well as ensuring a similar spatial domain (14.5°N - 15.0°N, 120.75°E -
169 121.25°E) to the MERRA-2 dataset.

170 2.1.5 NAAPS

171 Archived total and speciated optical depths along with surface concentrations of sulfate, dust,
172 and smoke are used from the Navy Aerosol Analysis and Prediction System (NAAPS:
173 1/3° × 1/3° spatial resolution) (Lynch et al., 2016), which is publicly available at
174 <https://www.nrlmry.navy.mil/aerosol/>. This reanalysis product relies on the Navy Global
175 Environmental Model (NAVGEM) for meteorological fields (Hogan et al., 2014). Hourly maps
176 were downloaded for Southeast Asia for aerosol particle events of interest based on AERONET
177 data. These maps help in the identification of regional emission sources.

178 2.1.6 NASA Worldview

179 Archived maps of cloud fraction (Aqua MODIS and Terra MODIS) were downloaded from
180 NASA Worldview (<https://worldview.earthdata.nasa.gov>) for events of interest based on
181 AERONET data.

182

183 2.2 Clustering

184 Available AERONET VSD data (0.050 μm to 15.000 μm particle radius in 22 logarithmically
185 equidistant bins, 1419 data points) were clustered via k-means clustering (Lloyd, 1982). The
186 algorithm used was k-means++ (Arthur and Vassilvitskii, 2006). The ideal number of clusters
187 was chosen based on relatively highest (>0.5) average silhouette value and the presence of a
188 cluster with a second peak in the larger accumulation mode of the VSD. The clusters were



189 analyzed based on their associated meteorological conditions and aerosol particle characteristics
 190 and were classified into air mass types (Table 2) based on previous studies (Pace et al., 2006;
 191 Kaskaoutis et al., 2007; Sorooshian et al., 2013; Kumar et al., 2014; Sharma et al., 2014; Che et
 192 al., 2015; Kumar et al., 2015).

193 **Table 2:** Summary of threshold values of aerosol optical depth (AOD), angstrom exponent (AE),
 194 and fine mode fraction (FMF) used to identify air mass types.

Air Mass Type	AOD	AE	FMF	Source
Clean Fine	< 0.1	> 1	> 0.7	Sorooshian et al., 2013
Polluted Fine	> 0.1	> 1	> 0.7	Sorooshian et al., 2013
Clean Coarse	< 0.1	< 1	< 0.3	Sorooshian et al., 2013
Polluted Coarse	> 0.1	< 1	< 0.3	Sorooshian et al., 2013
Desert Dust	> 0.3	-	< 0.6	Kaskaoutis et al., 2007
Clean Marine	< 0.2	-	< 0.7	Kaskaoutis et al., 2007
Urban/Industrial	> 0.2	-	> 0.8	Kaskaoutis et al., 2007

195

196 **2.3 Extreme Event Analysis**

197 Selected types of aerosol particle events were identified to characterize different types of sources
 198 and processes impacting aerosol particle columnar properties above Metro Manila. The three
 199 events are described below.

200 2.3.1 Smoke Long Range Transport

201 Events related to transported biomass burning/smoke were chosen based on the highest black
 202 carbon contribution to total AOD from the MERRA-2 dataset, high smoke contributions to AOD
 203 from NAAPS, and a dominant submicrometer peak in the AERONET VSD (Eck et al., 1999)
 204 over Metro Manila. Maps of surface smoke contributions from NAAPS as well as back-
 205 trajectories from the National Oceanic and Atmospheric Administration’s (NOAA) Hybrid
 206 Single-Particle Lagrangian Integrated Trajectory (HYSPLIT) model (Stein et al., 2015; Rolph et
 207 al., 2017) were used to identify the likely source and transport pathway for the smoke cases.
 208 Three-day back-trajectories with six-hour resolution were generated based on the NCEP/NCAR
 209 reanalysis meteorological dataset and with a resolution of 1° and a vertical wind setting of
 210 “model vertical velocity”. Trajectories were computed for an end point with an altitude of 500 m
 211 above ground level at the Manila Observatory. This altitude represents the mixed layer based on
 212 related surface air quality studies (Crosbie et al., 2014; Mora et al., 2017; Schlosser et al., 2017;
 213 Aldhaif et al., 2020), including a previous study for the same area (Stahl et al., 2020).

214 2.3.2 Dust Long Range Transport

215 A dust transport case was identified based on the highest dust contribution to AOD from the
 216 MERRA-2 dataset, high dust contributions to AOD from NAAPS, and an enhanced coarse peak
 217 in the AERONET VSD (compared to the submicrometer fraction) (Eck et al., 1999) over Metro
 218 Manila. Surface dust concentrations from NAAPS along with HYSPLIT back-trajectories
 219 confirmed the plausibility of dust for this case.

220 2.3.3 Cloud Processing



221 Cloud processing events were identified based on bimodal submicrometer VSDs (Eck et al.,
222 2012) and a relatively large sulfate contribution to AOD over Metro Manila from the MERRA-2
223 dataset, since this species is predominantly produced via cloud processing (Barth et al., 2000;
224 Faloon, 2009). The presence of clouds was verified with imagery from NASA Worldview in the
225 path of air parcels reaching Metro Manila based on HYSPLIT back-trajectories.
226

227 **2.4 Empirical Orthogonal Functions**

228 Empirical orthogonal function (EOF) analysis was performed to be able to associate the air mass
229 clusters identified earlier with regional scale aerosol particle sources. EOF analysis was done on
230 the monthly AOD data (January 2009 to December 2018) from MERRA-2 for the Southeast Asia
231 region for the months similar in scope to the AERONET data. EOF analysis needs a complete
232 dataset with no data gaps, which is not available with pure satellite retrievals; MERRA-2
233 reanalysis data alleviate this issue.

234 The monthly MERRA-2 AOD maps (0° - 30° N, 105° E – 135° E with 0.5° latitude and 0.625°
235 longitude resolution) (Lat: 61 rows x Lon: 49 columns) for the Southeast Asia region (presented
236 subsequently) were first deseasonalized. Then, the AOD anomaly per grid per year (of the 120
237 months) was calculated by subtracting the monthly mean AOD from each value of a given month
238 (Li et al., 2013). The anomalies per grid were weighted depending on their latitude by
239 multiplying the anomalies by the square root of the cosine of their latitudes.

240 EOF, specifically singular value decomposition (SVD), analysis (Björnsson and Venegas, 1997)
241 was then performed. To prepare the data for the analysis, they were transformed such that the
242 final matrix was a 2D matrix (120 x 2989) with each row representing a year, and each column
243 representing a grid in the map. The matrix was analyzed for eigenvalues using SVD in Matlab,
244 which outputted the eigenvalue (S) and eigenvector (U: principal components and V: empirical
245 orthogonal functions) matrices. The eigenvalues were, by default, arranged in descending order.
246 Each PC time series was standardized by dividing each PC value by the standard deviation per
247 PC time series (120 months).

248 An eigenvalue spectrum was also plotted based on the variance explained by each eigenvalue
249 and error bars that were calculated using the North test (North et al., 1982). Then, the
250 unweighted AOD anomalies were regressed onto the first three standardized PCs. Each grid
251 therefore had a regression between 120 pairs (unweighted AOD anomalies vs standardized PCs).
252 From the linear regression equation, the regression coefficient per grid was calculated and
253 plotted.
254

255 **2.5 Correlations**

256 The first three standardized PCs of AOD anomalies were correlated to deseasonalized
257 compositional AOD fractions (Sulfate, BC, OC, Dust, and Sea Salt). For each correlation, the t-
258 test value was calculated, and the resulting t-score was compared to a t-critical value for $\sim n=100$
259 pairs (n is the number of pairs of data, in this case 120 months) for 0.90 confidence level, which
260 is 1.660. Correlations that have t-values exceeding +1.660 or less than -1.660 (two-tailed test) are
261 significant (90% confidence).
262

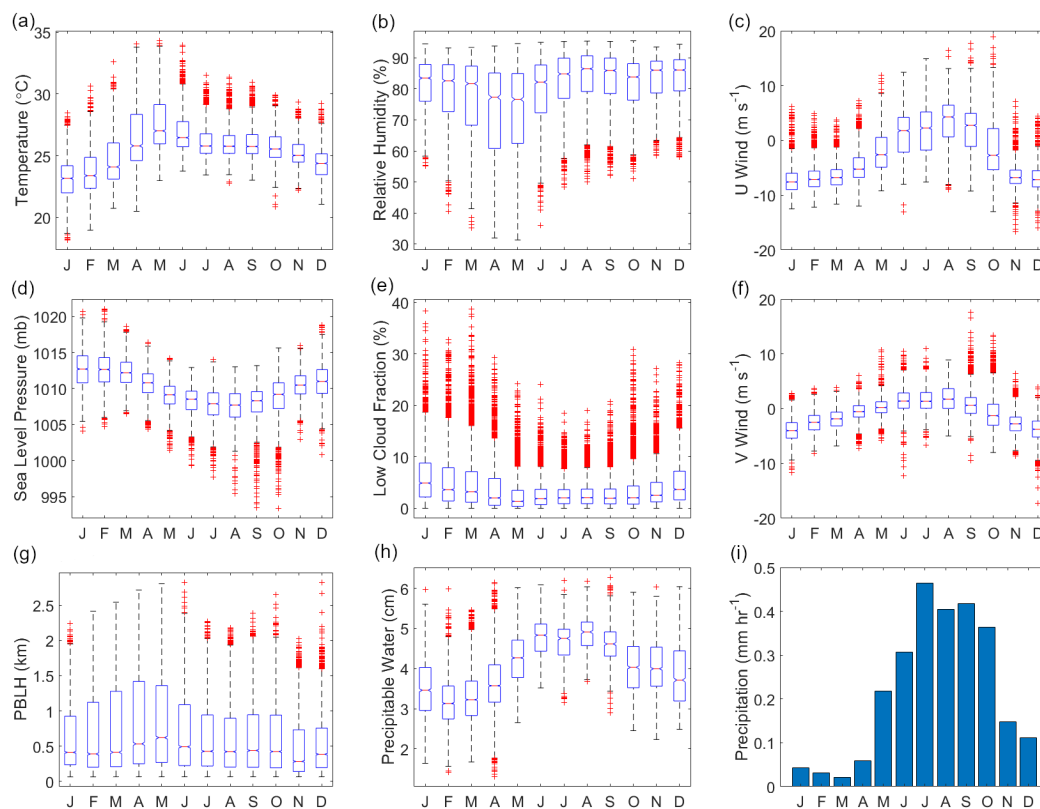


263 3 Results and Discussion

264 3.1 Meteorology and Atmospheric Circulation

265 Knowledge of monthly behavior of weather in the study region helps interpretation of aerosol
266 particle data. Philippine climate is influenced both by the winter northeast monsoon
267 (~November to April, Amihan) and the summer southwest monsoon (~May to October, Habagat)
268 (Coronas, 1920; Flores, 1969; Matsumoto et al., 2020). Median 3-hourly temperatures per month
269 (MERRA-2, 975 mb) (Fig. 1a) ranged from 23.2 °C in January during the winter northeast
270 monsoon, to 27.0 °C in May during the transition from the summer season, as defined in
271 (Bañares et al., 2021), to the southwest monsoon. May was also the month with the lowest
272 median 3-hourly relative humidity (76.6%) (MERRA-2, 975 mb) (Fig. 1b). The highest median
273 level of relative humidity for a month was in August (86.5 %) during the summer southwest
274 monsoon, which is also the time of the year (June to August) when rainfall peaks in the region
275 where the sampling station (Manila Observatory) is located (Coronas, 1920; Cruz et al., 2013).
276 The highest mean hourly precipitation (Fig. 1i) per month was from July (0.46 mm hr⁻¹) to
277 September (0.42 mm hr⁻¹), while March exhibited the lowest mean hourly rainfall (0.02 mm hr⁻¹).
278 Like relative humidity and precipitation, median precipitable water (from available
279 AERONET data) (Fig. 1h) was highest in August (4.9 cm) and lowest in February and March
280 (3.1 cm and 3.2 cm, respectively).

281



282

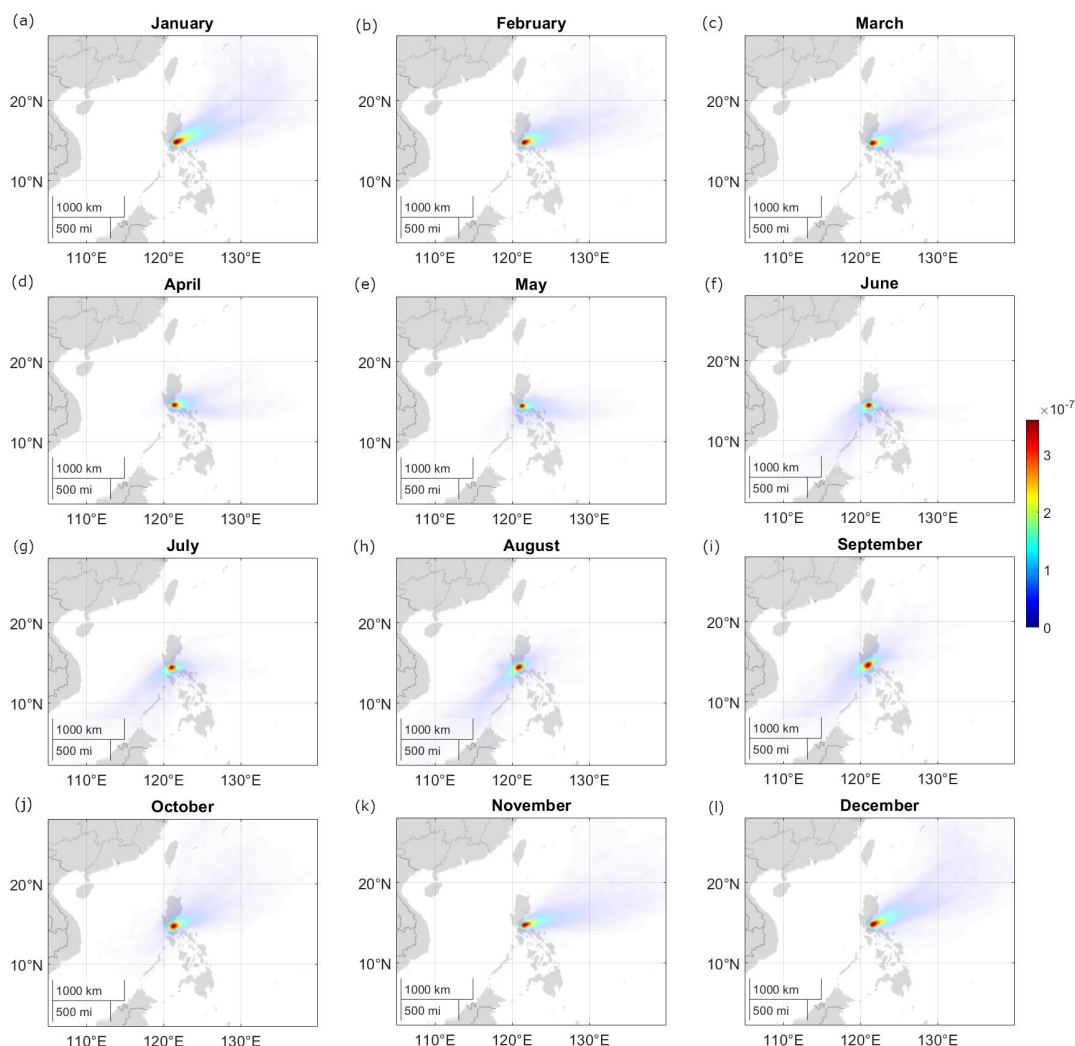
283



284 **Figure 1:** Monthly characteristics of meteorological parameters for Metro Manila, Philippines
285 based on data between January 2009 and October 2018. MERRA-2 parameters: (a) temperature,
286 (b) relative humidity, (c/f) u and v wind at 975 mb, (d) sea level pressure, (g) planetary boundary
287 layer height (PBLH), (e) low cloud fraction; AERONET: (h) precipitable water; PERSIANN: (i)
288 mean hourly precipitation per month.
289

290 The lowest 3-hourly median pressures (MERRA-2) were observed (Fig. 1d) between July and
291 September during the southwest monsoon season (~985.2 – 985.8 mb). This is also the time
292 when the most number of tropical cyclones pass the island of Luzon (Wu and Choy, 2016). The
293 highest 3-hourly median pressures (988.1 – 990.0 mb) were during the winter northeast
294 monsoon.

295 Median winds (MERRA-2) were from the south/southwest direction from June to September
296 (Fig. 1c and 1f), associated with the summer southwesterly monsoon. HYSPLIT back-
297 trajectories show the same wind pattern (Fig. 2f to 2i). The highest median 3-hourly wind speeds
298 (MERRA-2) (Fig. 1c and 1f) during the southwest monsoon were recorded for August (u: 4.2 m
299 s^{-1} and v: 1.7 $m s^{-1}$). Median winds begin to transition in October and November (to the northeast
300 monsoon: Amihan) (Fig. 2j and 2k) coming from the east/northeast and maintained until
301 February (Fig. 2b), which is towards the end of the winter northeast monsoon. There were
302 generally higher wind speeds and the highest median 3-hourly wind speeds of the year
303 (MERRA-2) (Fig. 1c and 1d) in January (u: -7.6 $m s^{-1}$ and v: -4.0 $m s^{-1}$). Median winds shifted
304 toward a more easterly source from March to May (transition time before the Habagat monsoon)
305 (Fig. 2c to 2e) accompanied by decreasing median 3-hourly wind speeds (u = -6.8 $m s^{-1}$, v = -1.9
306 $m s^{-1}$ to u: -2.6 $m s^{-1}$, v = 0.2 $m s^{-1}$).



307
308
309

Figure 2: Density plots of trajectories reaching Manila Observatory per month from 2009 to 2018.

310 The transition times between the monsoons (when the wind directions shift and wind speeds
311 change) are also the times of the highest (May, Fig. 1g, 621.2 m) and lowest (November, Fig. 1g,
312 279.6 m) median planetary boundary layer heights (MERRA-2). The median planetary boundary
313 layer height was highest during the period (May) of highest temperatures, lowest relative
314 humidity, reduced air pressure, and lowest monthly median low cloud fraction (MERRA-2) (Fig.
315 1e) (1.4 %). The lowest monthly median planetary boundary layer height was observed during
316 the period (November) when temperatures were beginning to cool and air pressure was rising.
317 The monthly maximum low cloud fraction was lowest in July (18.5 %) during the summer
318 southwest monsoon while the monthly median and monthly maximum low cloud fractions



319 (MERRA-2) (Fig. 1e) were highest (38.3 % max, 4.9 % median) in January during the winter
 320 northeast monsoon.

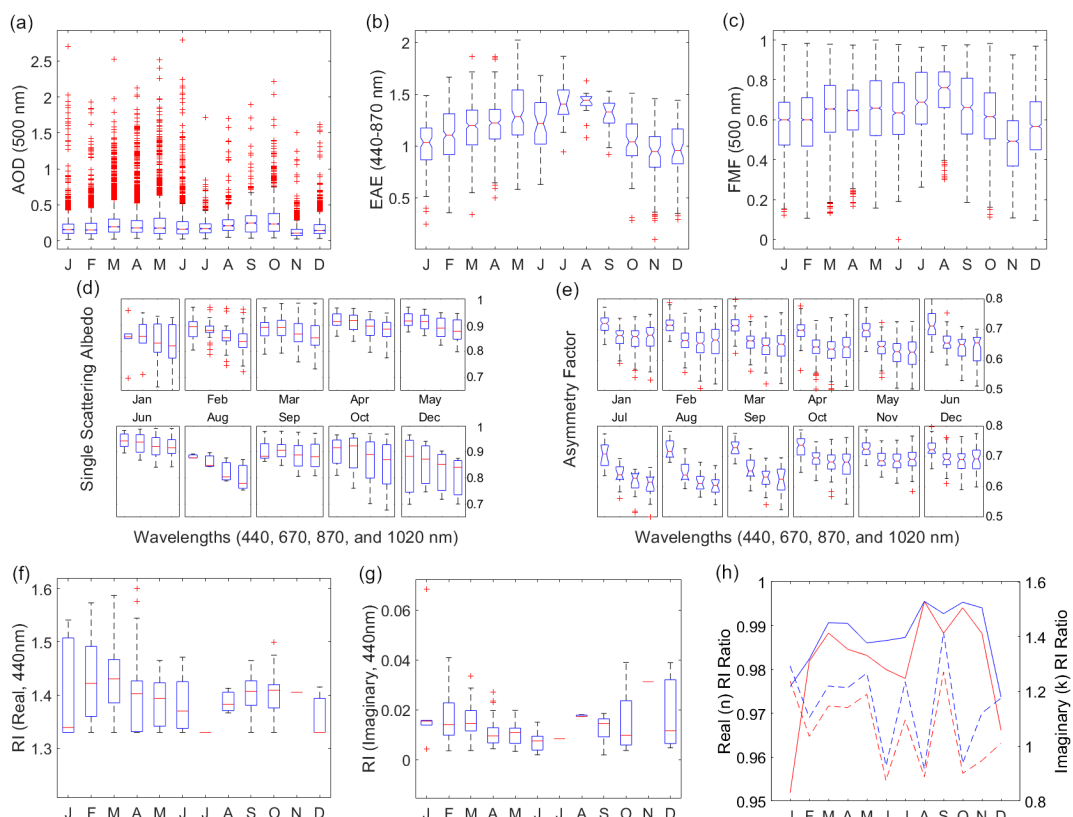
321

322 3.2 Aerosol Particle Characteristics

323 3.2.1 Aerosol Optical Depth

324 Monthly median AOD (AERONET) (Fig. 3a) over the Manila Observatory was highest from
 325 August (0.21) to October (0.23) around the time of the summer monsoon when winds were
 326 coming from the southwest (Figs. 2h to 2i) (Holben et al., 2001). This is the same time of year
 327 when biomass burning activities occur in the region southwest of Metro Manila. AOD over the
 328 larger Southeast Asia region from MISR and MERRA-2 (Fig. 4) had a similarly large peak from
 329 September to October which, however, was second only in magnitude to a March peak, which is
 330 influenced by biomass burning in Peninsular Southeast Asia (PSEA) (Gautam et al., 2013; Hyer
 331 et al., 2013). This larger peak in March, attributed to PSEA west of the Philippines, was not as
 332 prevalent in the AERONET AOD data due to the dominant easterly winds in the Philippines in
 333 March (Fig. 2c) and more localized sources.

334



335

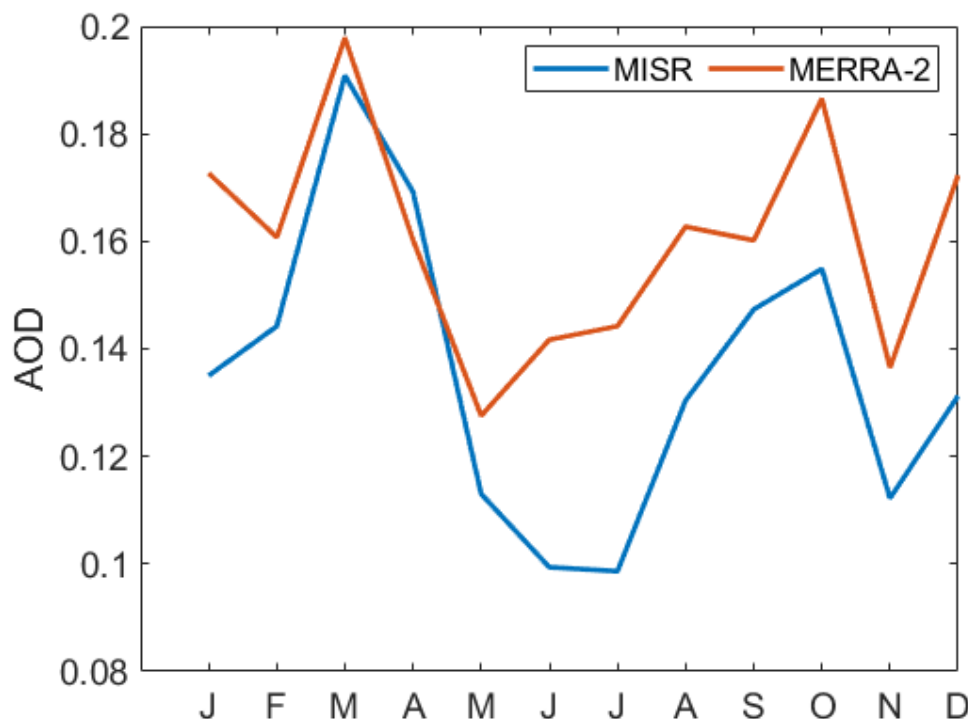
336 **Figure 3:** Monthly characteristics of AERONET aerosol particle parameters: (a) aerosol optical
 337 depth (AOD), (b) extinction angstrom exponent (EAE), (c) fine mode fraction (FMF), (d) single
 338 scattering albedo (SSA), (e) asymmetry factor (AF), (f) real and (g) imaginary refractive index
 339 (RI) values (440 nm), and (h) refractive index ratios (where the blue line is the ratio of RI at 440



340 nm and 675 nm, the red line is the ratio of RI at 440 nm and the average RI for the 670–1020 nm
341 wavelengths, and the broken lines are the imaginary refractive index ratios) for Metro Manila,
342 Philippines based on data between January 2009 and October 2018.

343 There is a notable dip in the monthly median AERONET AOD from the peak in October to the
344 lowest monthly median AOD (0.11) in November, just slightly above defined background levels
345 (<0.1) (Holben et al., 2001), when the windspeeds were picking up and were coming from the
346 east to northeast directions (Fig. 2k) in the direction of the Philippine Sea and the West Pacific
347 Ocean. This dip was also observed in the regional AOD data (MISR and MERRA-2, Fig. 4).

348



349

350 **Figure 4:** Monthly median AOD in Southeast Asia from 2009 to 2018 from MISR (blue line)
351 and MERRA-2 (red line).

352 There were 338 instances (~1.2 % of the time based on the total number of 28,538 valid
353 AERONET AOD data points) of AOD values exceeding 1, indicative of heavy aerosol particle
354 loading (Huang et al., 2021). Because AOD is extrinsic (it depends on mass), AOD describes
355 total aerosol particle loading and we examine other aerosol particle parameters from AERONET
356 to make more informed inferences about size and composition.

357 3.2.2 Extinction Angstrom Exponent and Fine Mode Fraction



358 The extinction angstrom exponent (EAE) relates the extinction of light at specific wavelengths
359 and is indicative of aerosol particle size (Ångström, 1929). The EAE is usually greater for
360 smaller particles (~4 for very small particles that undergo Rayleigh scattering and 0 for particles
361 as large as cloud drops) (Bergstrom et al., 2007), except for when the coarse mode has a large
362 impact on the angstrom exponent (Schuster et al., 2006). The highest monthly median EAE (Fig.
363 3b) from 2009 to 2018 over the Manila Observatory was observed from July (~1.4) to September
364 (~1.3), during the southwest monsoon. This period is associated with the biomass burning
365 southwest of the Philippines (Oanh et al., 2018; Stahl et al., 2021; Crosbie et al., 2022). The
366 median (per month) EAE ranged from ~0.9 in November to ~1.4 in August, a range which is
367 within the values from previous studies collected from mixed sites and urban/industrial areas
368 with both fine and coarse particles (Eck et al., 2005; Giles et al., 2012).

369 EAE increases with AOD (Fig. S1), which means that the greater particle loading is contributed
370 by smaller particles (Smirnov et al., 2002). Of the high loading cases (AOD >1), the EAE values
371 ranged from 0.6 to 1.6, indicating fine mode particles (Che et al., 2015). The EAE values in
372 August were the highest compared to other months including having the highest minimum value
373 of any month (0.71) (Fig. S1), due to smaller particles (~EAE >1 for fine particles, Table 2).
374 The lowest EAE values (0.08) and thus the largest particles were observed in December.

375 The fine mode fraction (FMF) describes the prevalence of fine mode particles in the column of
376 air above the surface. The fine mode fraction (Fig. 3c) from 2009 to 2018 was highest in August
377 (monthly median of 0.75) and lowest in November (monthly median of 0.45). This is consistent
378 with the EAE values discussed earlier with the prevalence of smaller particles in August and
379 larger particles in November. In August (Fig. 2h) the southwest monsoon is known to coincide
380 with transported fine smoke particles to Luzon. In November (Fig. 2k), the prevalent winds may
381 have already shifted to easterly (Matsumoto et al., 2020) implying more marine-related sources
382 associated with coarser particles.

383 3.2.3 Single Scattering Albedo

384 The single scattering albedo (SSA) is the most important aerosol particle parameter determining
385 whether aerosol particles will have a warming or cooling effect (Reid et al., 1998). SSA is the
386 ratio of the scattering coefficient to the total extinction (scattering and absorption) coefficient
387 (Bohren and Clothiaux, 2006) of aerosol particles. Higher SSAs are related to more reflective
388 aerosol particles while more absorbing aerosol particles will have lower SSA values; values
389 range from 1 (reflective) to 0 (absorbing). Monthly median SSA values were largest in June
390 (0.94, 440 nm), suggesting the presence of more reflective aerosol particles, and smallest in
391 August (0.78, 1020 nm). August is when biomass burning is prevalent to the southwest of the
392 Philippines and associated with soot particles that are absorptive.

393 The sensitivity of SSA to different wavelengths depends on the type of aerosol particles present.
394 More specifically, aerosol particle size and refractive index (which is related to aerosol particle
395 composition) both affect the SSA (Dubovik and King, 2000; Bergstrom et al., 2007; Moosmüller
396 and Sorensen, 2018). For dust-type particles, SSA increases with wavelength because of lower
397 dust absorption in the higher visible to infrared wavelengths (Dubovik et al., 2002), while for
398 urban particles (including black carbon), which absorb light at longer wavelengths, SSA
399 decreases with wavelength (Reid et al., 1998; Bergstrom et al., 2002). The presence of organic
400 carbon may affect this spectral dependence; however, because organic particles absorb in the



401 UV, this lowers SSA at wavelengths shorter than 440 nm (Kirchstetter et al., 2004). Monthly
402 median SSA generally decreased with increasing wavelength for all months with available data
403 (Fig. 3d) presumably due to the influence of more urban particles in contrast to dust.
404 Noteworthy though are the monsoon transition months of April, September, and October (Fig.
405 3d), which had increased SSA from 440 nm to 670 nm, possibly from organics along with black
406 carbon due to transported smoke. The back-trajectories for these months (Figs. 2d, 2i, and 2j)
407 suggest sources from the northeast that are closer to Luzon during these months compared to
408 other months. This indicates the possibility of more local sources. Increasing the certainty of
409 sources associated with aerosol particles necessitates looking at other available aerosol particle
410 parameters, discussed subsequently.

411 3.2.4 Asymmetry Factor

412 The asymmetry factor quantifies the direction of scattering of light due to aerosol particles, with
413 values ranging from -1 (back scatter) to 0 (uniform scattering) to 1 (forward scatter). It is
414 important in modeling climate forcing because it affects the vertical distribution of the radiation
415 in the atmosphere (Kudo et al., 2016; Zhao et al., 2018). The asymmetry factor is dependent on
416 particle size, shape, and composition and the value of 0.7 is used in radiative models (Pandolfi et
417 al., 2018).

418 Lower asymmetry factors are related to smaller particles (at constant AOD) (Bi et al., 2014).
419 Measured values due to biomass burning, for example, are 0.54 (550 nm) in Brazil (Ross et al.,
420 1998) and 0.45 – 0.53 (550 nm and including dust) over central India (Jose et al., 2016). There
421 have been relatively higher values observed in western, central, and eastern Europe (0.57 – 0.61
422 at 520 – 550 nm) (Pandolfi et al., 2018) and the U.S. East Coast (0.7 at 550 nm) (Hartley and
423 Hobbs, 2001). In Norway, the asymmetry factor for background summer conditions was 0.62
424 and was higher in the springtime at 0.81 (862 nm) during Arctic haze events (Herber et al.,
425 2002). Highest values are associated with dust such as those measured in the Sahara being 0.72 –
426 0.73 (500 nm) (Formenti et al., 2000). Over Metro Manila, the asymmetry factors from the
427 AERONET data at the 675, 870, and 1020 nm were similar across months (Fig. 3e). The monthly
428 median asymmetry factors at 440 nm ranged from 0.70 (April and May) to 0.74 (October), while
429 for 670, 870, and 1020 nm the monthly median asymmetry factors were smaller and ranged from
430 0.62 – 0.69. These values were closely related to those observed over the U.S. East Coast as
431 mentioned earlier, perhaps due to the proximity of the location to the coast (10 km east of Manila
432 Bay and 100 km west of the Philippine Sea) as well as its location in Manila, which is a large
433 local source due mostly to vehicles (Cruz et al., 2019).

434 The monthly median asymmetry factor in Metro Manila was greatest towards the end of the year
435 (October to December) for all the wavelengths, suggesting larger particles when winds (Figs. 2j
436 to 2l) come from the Philippine Sea in the northeast. It was in March and April that the monthly
437 median asymmetry factor was minimal for 440 nm and in August for 670, 870, and 1020 nm.
438 These were the times when the aerosol particles were smallest. March to April represents the
439 driest time of the year in Manila (Fig. 1b and 1h) perhaps preventing particle growth and where
440 the local sources may be dominating, even as back-trajectories (Fig. 2c and 2d) extend all the
441 way from the Philippine Sea to the east. This is corroborated by results from other studies
442 showing that the asymmetry factor seems to be enhanced by relative humidity (Zhao et al.,
443 2018). The unexpected low asymmetry factor values in August, however, are probably because
444 of the source of the particles. August had the highest relative humidity and precipitable water



445 (Fig. 1b and 1h) but is also when the back-trajectories (Fig. 2h) were from the southwest,
446 possibly affected by the Indonesia fires, which could have transported more non-hygroscopic
447 fine particles.

448 Fine particles have been observed to exhibit decreasing asymmetry factors with increasing
449 wavelength (Bergstrom et al., 2003). This trend is observed in all the months for the monthly
450 median asymmetry factors (Fig. 3e) suggesting the predominance of smaller aerosol particles.
451 The greatest decrease in the asymmetry factor (all wavelengths) was in August, consistent with
452 the lowest observed values of the year (670, 870, and 1020 nm). Transported biomass burning
453 particles are the probable dominant particles during this time. They are usually composed of
454 hygroscopic inorganics, non-hygroscopic soot, and relative non-hygroscopic organic fractions
455 (Petters et al., 2009). Knowing the composition of biomass burning particles over the study
456 region will help in the understanding of hygroscopicity and its impacts on radiation.

457 3.2.5 Refractive Index

458 Refractive index is an intrinsic parameter as it does not depend on the mass or the size of
459 particles, and thus can be used to infer aerosol particle composition (Schuster et al., 2016).
460 Refractive index measurements are complex since they include real and imaginary parts related
461 to light scattering and absorption, respectively. All aerosol particles scatter light but only certain
462 types absorb light significantly. The most prominent particle absorbers in the atmosphere are
463 soot carbon, brown carbon (organic carbon that absorbs light), and free iron from dust (hematite
464 and goethite in the ultraviolet to mid-visible) (Schuster et al., 2016). For this study, we examine
465 refractive index values at 440 nm wavelength because this is the wavelength used to calculate
466 SSA (Andrews et al., 2017). Pure sources of soot carbon have the highest real refractive index
467 values (~1.85) as well as the highest imaginary refractive index (~0.71), both independent of
468 wavelength (Koven and Fung, 2006; Van Beelen et al., 2014). Brown carbon and dust have
469 relatively lower real refractive index values at 440 nm (~1.57 and ~1.54) and imaginary
470 refractive index values (~0.063 and ~0.008) that decrease with increasing wavelength (Xie et al.,
471 2017).

472 In this study the range of the monthly median real refractive index values (440 nm) was from
473 1.33 (December and January) to 1.43 (March) (Fig. 3f). Water uptake by aerosol particles
474 decreases the real refractive index values (Xie et al., 2017) and thus the lowered real refractive
475 indices over the Manila Observatory can be due to the presence of more water in the atmosphere
476 in general and/or the increased presence of more hygroscopic particles. December and January
477 are not necessarily the months that have the highest moisture content, but they are months when
478 back-trajectories reaching the column over the Manila Observatory are from the Philippine Sea
479 to the northeast presumably transporting hygroscopic particles. As reported in previous sections,
480 relatively larger particles are observed around this time of the year and thus sea salt can be an
481 important contributor. The greatest change in the monthly median real refractive index with
482 increasing wavelength also was observed in December (Fig. 3h), possibly due the increased
483 fractional contribution of constituents other than soot carbon (because the real refractive index of
484 soot carbon is invariant with wavelength). Noteworthy as well is the month of August (Fig. 3f),
485 which has the smallest range of real refractive index values, possibly indicating a more
486 homogenous aerosol particle source compared to other months. August is the month with the
487 highest relative humidity (Fig. 1b) as well as highest precipitable water (Fig. 1h), while this is



488 also the month when long-range biomass burning emissions are observed to be highest, and
489 when the real refractive index values would otherwise be expected to be highest.

490 Water content seems to play a significant role in the real refractive index values in Manila.
491 March, when the monthly median real refractive index values are highest (Fig. 3f), is when
492 precipitable water vapor (Fig. 1h) is among the lowest in the year. The months around March are
493 also when maximum real refractive indices (1.57 in February, 1.59 in March, and 1.60 in April)
494 were observed (Fig. 3f). March was when there was a relatively small change in real refractive
495 index value with wavelength perhaps related to greater soot carbon fractions during this time,
496 due possibly to the contribution of biomass burning from Peninsular Southeast Asia (Shen et al.,
497 2014). Looking more closely at the imaginary refractive index values will help elucidate this
498 issue.

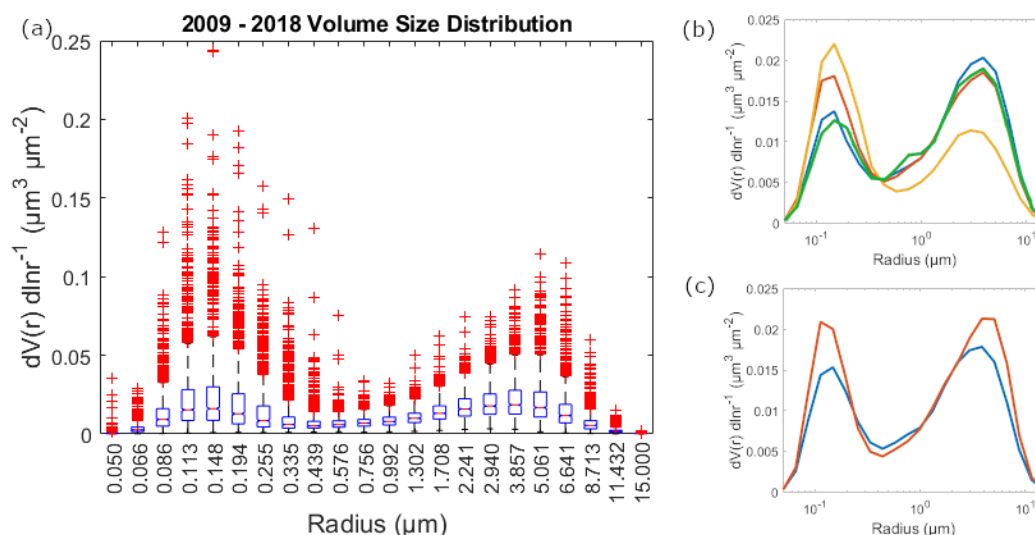
499 Monthly median imaginary refractive index values (440 nm) ranged from 0.007 in June to 0.015
500 in September and December (Fig. 3g). These are low compared to those of the pure soot carbon
501 mentioned earlier because of the mixed nature of the sampling site with contributions from
502 brown carbon and dust. The highest imaginary refractive index values in September and
503 December suggest the greatest fractional contribution of soot because the highest imaginary
504 refractive index values are associated with soot. These are also similar in magnitude to biomass
505 burning particles in the Amazon (0.013) (Guyon et al., 2003). The key distinction between soot
506 carbon and other major absorbers (brown carbon and dust) is that its imaginary refractive index
507 is invariant with wavelength. Both brown carbon and dust exhibit a decrease in the imaginary
508 refractive index with increasing wavelength (Xie et al., 2017). The ratios of imaginary refractive
509 index values (440 nm to average of 670–1020 nm) (Fig. 3h) show a relative invariance with
510 wavelength (ranging from 0.88 to 1.4), which indicates the dominance of soot as the major
511 absorber in the region (Eck et al., 2003). While observed wavelength invariance points to high
512 soot contributions, the size of the particles can help distinguish between brown carbon, which
513 reside mainly in the fine mode, and dust sources, which yield more coarse particles (Schuster et
514 al., 2016). September is during the southwest monsoon, which is when, as noted in the earlier
515 sections, fine particles were most prevalent. This is also the time when the imaginary refractive
516 index varied most with wavelength (1.4 ratio of the imaginary refractive index at 440 nm and the
517 imaginary refractive index average for 670 nm to 1020 nm in Fig. 3h) possibly with greater
518 absolute contributions from brown carbon, even with the highest soot carbon fractional
519 contributions. Brown carbon has been observed both from primary and aged aerosol particle
520 emissions from biomass burning (Saleh et al., 2013). As noted earlier, December also had the
521 highest imaginary refractive index values as well as relatively coarser particles, possibly due to
522 larger dust absolute contributions even with the highest soot carbon fraction contributions. The
523 lowest monthly median imaginary refractive index values in June, on the other hand, when fine
524 mode particles prevail suggest highest fractional contributions of brown carbon relative to other
525 months (Fig. 3h).

526 3.2.6 Volume Size Distributions

527 The volume size distribution (VSD) is another way to be able to more deeply characterize
528 aerosol particles, specifically related to their effect on climate, weather, and clouds (Haywood
529 and Boucher, 2000; Feingold, 2003). In the Manila Observatory dataset, there was a bi-modal
530 VSD for the entire dataset (Fig. 5a). The fine mode median values peaked in the accumulation
531 mode at 0.148 μm particle radius while the coarse mode median values peaked at 3.857 μm . The



532 median coarse mode amplitudes were higher than the fine mode amplitudes for most of the year
 533 (DJF, MAM, and SON, Fig. 5b), except during the southwest monsoon (JJA) when the fine
 534 mode amplitude was higher. This is consistent with observations earlier of fine mode prevalence
 535 during the southwest monsoon. Median VSD amplitudes (Fig. 5c) were greater in the afternoon,
 536 with higher peaks for both the fine and coarse modes, compared to the morning. There was a
 537 slightly larger coarse median amplitude, compared to the accumulation mode median amplitude,
 538 for both the morning and afternoon size distributions. While the VSDs confirm several
 539 observations based on the analysis of the aerosol particle parameters presented earlier, not much
 540 further information is gained especially regarding chemical composition. Size distributions are a
 541 result of contributions from multiple sources, and thus being able to discriminate the sources
 542 based on their characteristic size distributions will help identify relevant sources.
 543



544

545 **Figure 5:** (a) VSD results derived from AERONET measurements at Metro Manila between
 546 January 2009 and October 2018. Median VSDs over the study period based on (b) season (blue:
 547 DJF, red: MAM, orange: JJA, green: SON) and (c) time of day (blue: AM, red: PM).

548

549 3.3 Clusters

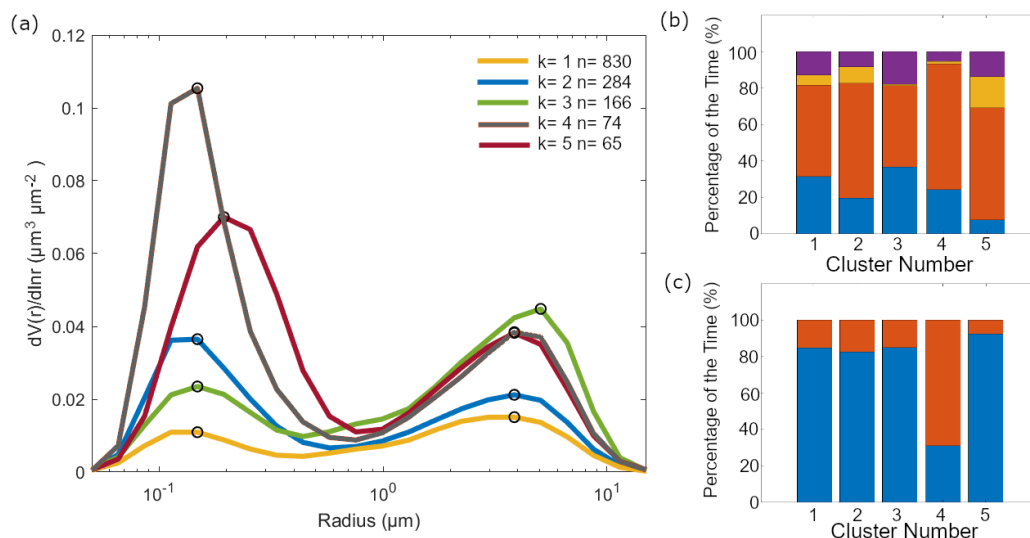
550 3.3.1 VSD Cluster Profiles

551 Five clusters were identified to best represent the VSD (Fig. 6a). The average of the VSDs in
 552 each cluster varied depending on the height of the peaks in the accumulation mode and the
 553 coarse mode. In Metro Manila, the accumulation mode is associated with aged aerosol particles
 554 and combustion (Cruz et al., 2019). The majority of the data (830 count out of 1419 total VSD
 555 profiles) were clustered together in a profile (cluster 1) that had relatively low average
 556 magnitudes for both the accumulation ($0.01 \mu\text{m}^3 \mu\text{m}^{-2}$) and coarse ($0.02 \mu\text{m}^3 \mu\text{m}^{-2}$) modes, with
 557 the magnitude of the coarse mode peak slightly higher than the magnitude of the accumulation
 558 mode. The next prevalent cluster profile (284 counts, cluster 2) had an average fine mode peak
 559 ($0.04 \mu\text{m}^3 \mu\text{m}^{-2}$) which was more than twice as much than the previous profile but with a similar
 560 coarse mode peak ($0.02 \mu\text{m}^3 \mu\text{m}^{-2}$). The average coarse mode peak ($0.04 \mu\text{m}^3 \mu\text{m}^{-2}$) was the



561 highest (compared to the four other cluster profiles) for the third prevalent cluster profile (166
 562 counts, cluster 3); cluster 3 was also slightly shifted in the coarse mode to a higher radius (5.06
 563 μm) compared to other clusters. The coarse mode dominated this VSD compared to other
 564 profiles (lower magnitude for the accumulation mode peak, $0.02 \mu\text{m}^3 \mu\text{m}^{-2}$). The two remaining
 565 cluster profiles exhibited high average magnitudes in both the accumulation and coarse modes.
 566 The fourth prevalent cluster profile (74 counts, cluster 4) had the highest average absolute
 567 magnitude in the accumulation mode ($0.11 \mu\text{m}^3 \mu\text{m}^{-2}$), while the fifth prevalent cluster profile
 568 (65 counts, cluster 5) had a slightly smaller accumulation mode peak ($0.07 \mu\text{m}^3 \mu\text{m}^{-2}$) that was
 569 shifted to a slightly higher radius ($0.19 \mu\text{m}$ compared to $0.15 \mu\text{m}$). Both clusters 4 and 5 had
 570 similar average coarse mode peak magnitudes ($0.04 \mu\text{m}^3 \mu\text{m}^{-2}$).

571



572

573 **Figure 6:** (a) Cluster analysis of VSD data yielding five characteristic and averaged VSDs with
 574 the number of points per cluster shown in the legend. The black circles on the curves show the
 575 peak locations in the submicrometer ($<1 \mu\text{m}$) and coarse ($\geq 1 \mu\text{m}$) modes. The relative abundance
 576 of each cluster is shown for different (b) seasons (blue: DJF, red: MAM, orange: JJA, violet:
 577 SON) and (c) times of day (blue: AM, red: PM).

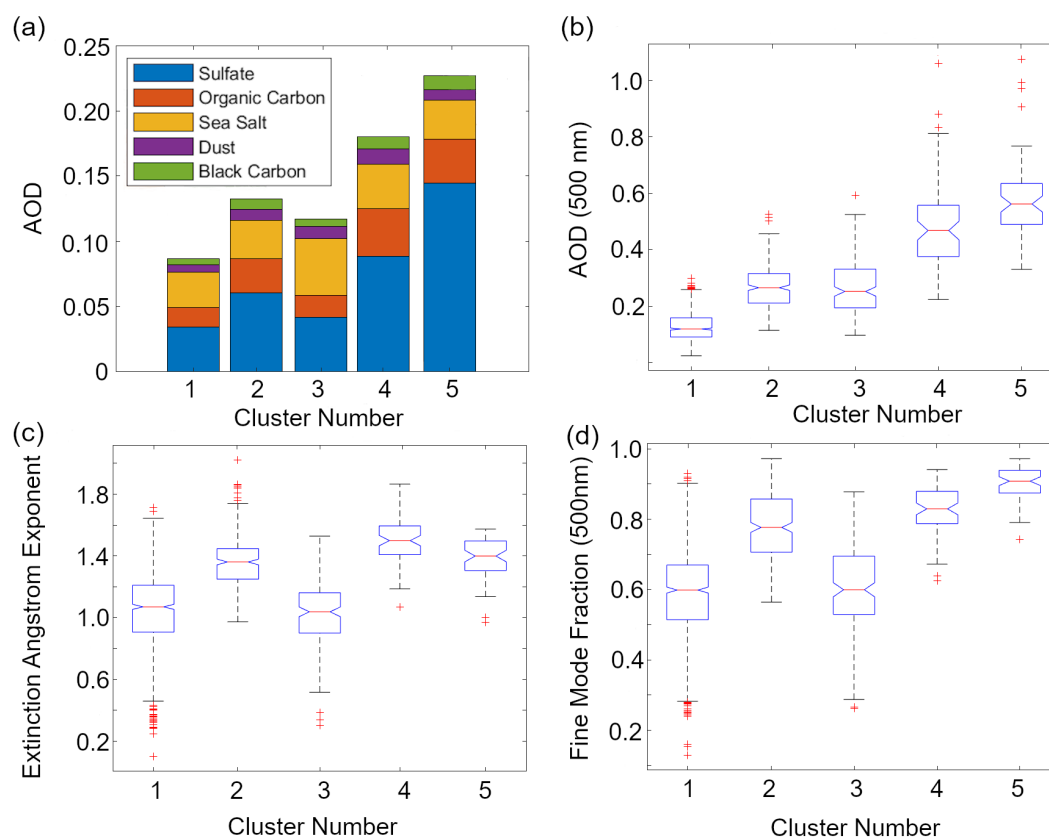
578 The clusters were distributed across seasons (Fig. 6b), with clusters 1 and 2 being the most
 579 evenly distributed among the clusters. Cluster 3, which had the highest coarse mode peak, had
 580 the greatest contribution from September to November compared to other clusters. Cluster 4,
 581 which had the highest accumulated mode peak compared to other clusters, had the greatest
 582 contribution from March to May as well as to afternoon VSDs compared to other clusters (Fig.
 583 6b and 6c). Relative contributions of VSDs from June to August were highest for cluster 5,
 584 which had the shifted accumulated mode peak.

585 Median total (AERONET) AOD values (Fig. 7b) were lowest (0.12) for cluster 1, though it had
 586 the second highest sea salt fractional contributions (Fig. 7a) to total AOD (MERRA-2) (31%)



587 among all the clusters. Cluster 2 had relatively mid-range median total AOD values (0.27) that,
 588 along with clusters 4 and 5, were dominated by sulfate and organic carbon (46% and 20%).
 589 Cluster 3 had similar, but slightly lower median total AOD (0.25) compared to cluster 2. Cluster
 590 3 was distinct because it had the largest total (0.04) and fractional contribution (37%) from sea
 591 salt among all clusters. Clusters 4 and 5 had the highest median total AOD values (0.47 and
 592 0.56), with cluster 5 having the highest absolute and fractional sulfate contributions (0.14 and
 593 64%) among the clusters. Integrating the above results with their corresponding aerosol particle
 594 properties can help associate the clusters to air masses.

595



596

597

598 **Figure 7:** (a) Average compositional contributions to aerosol optical depth (AOD) from
 599 MERRA-2 per identified cluster. Boxplots of AERONET (b) total AOD (500 nm), (c) extinction
 600 angstrom exponent (EAE, 440 nm – 870 nm total), and (d) fine mode fraction (FMF, 500 nm)
 601 per cluster.

602

3.3.2 Air Mass Types

603

604

605

Air masses have been classified in previous studies based on their AOD, EAE, and FMF values (e.g., Aldhaif et al, 2021). The criteria from different studies (Table 2) were applied per cluster. Median total AOD of cluster 1 (0.12) was less than 0.2 (Fig. 7b), which is the threshold for sea



606 salt sources (Kaskaoutis et al., 2007). Half of the data points in cluster 1 also fall below the
607 threshold for clean environments ($AOD < 0.1$) (Sorooshian et al., 2013). Based on its median
608 FMF (0.60) and EAE (1.07, where $EAE < 1$ is coarse and $EAE > 1$ is fine) values (Fig. 7c and
609 7d), cluster 1 is a mixture of fine and coarse particles. Cluster 1 is the only cluster with a median
610 that meets that threshold value for clean marine sources ($AOD < 0.2$), and we know from Sect.
611 3.3.1 that its average VSD magnitude was greater for the coarse fraction and that its sea salt
612 contribution to total AOD was second greatest among the clusters. Thus, we can say that most
613 probably cluster 1 is a background clean marine source, since it also is predominant throughout
614 the seasons (Fig. 6b). This makes sense given the proximity of the ocean to Metro Manila from
615 both the east and the west.

616 Most of the data from the other clusters all fall in the polluted category (Table 2), based on their
617 median total AODs (>0.1) (Fig. 7b). Cluster 2 has a median FMF value of 0.78 (Fig. 7c), which
618 suggests that most of the particles in this air mass are in the fine fraction. They are, however, not
619 sufficiently dominant in the aerosol for them to be typical of urban/industrial sources. The
620 average VSDs (Fig. 6a) of cluster 2 similarly suggest that their relative accumulation mode
621 magnitude is higher than the coarse magnitude, but not much higher. Like cluster 1, cluster 2 is
622 also more evenly distributed across the seasons (Fig. 6b) and could be a fine polluted background
623 source. Metro Manila is a megacity with continuous and large amounts of sources that could be,
624 due to its proximity to the ocean, interacting with the background.

625 Based on its median EAE value (1.04) (Fig. 7d), cluster 3 is mixed but mostly in the coarse
626 fraction, consistent with its VSD profile (Fig. 6a) which has the highest coarse magnitude (FMF
627 = 0.60) compared to the other clusters. The contribution of data from September to February is
628 greatest in cluster 3, consistent with expected coarser particles during this period when the winds
629 are initially shifting from the southwest before becoming more northeasterly, as previously
630 noted. This air mass can be a mixed polluted air mass, which is possibly transported due to the
631 large sea salt contribution to total AOD (Sect. 3.3.1).

632 Both clusters 4 and 5 have median total FMF (0.83 and 0.91) (Fig. 7c) values exceeding the mark
633 (> 0.8 , Table 2) for urban/industrial air masses. Combining this and results from the previous
634 sections confirms that cluster 4 can be an urban/industrial source given that it had the highest
635 median accumulated mode peak and organic carbon contribution to total AOD among the
636 clusters.

637 Cluster 5 had the highest median total AOD and FMF values (Fig. 7c). It also had the highest
638 (Fig. 7a) sulfate contribution to total AOD as well as a shifted accumulation mode peak (Fig. 6a).
639 These characteristics suggest that cluster 5 is a possible cloud processing air mass (Eck et al.,
640 2012). The larger peak in the accumulation mode is possibly the cloud signature. Previous
641 studies have attributed this larger mode to cloud processing due to the conversion of SO_2 to
642 sulfate (Hoppel et al., 1994). Cloud processing is a major source of sulfate (Barth et al., 2000).

643 The distribution of the air masses based on the abundance of the VSD profiles per cluster suggest
644 prevalent clean marine (58% of the total VSD counts) and background fine polluted (20%) air
645 masses over Metro Manila. The mixed polluted (12%), urban/industrial (5%), and cloud
646 processing (5%) air masses contribute 22% all together. We can investigate more deeply and
647 look at specific case studies that can better describe the air masses identified here.



648

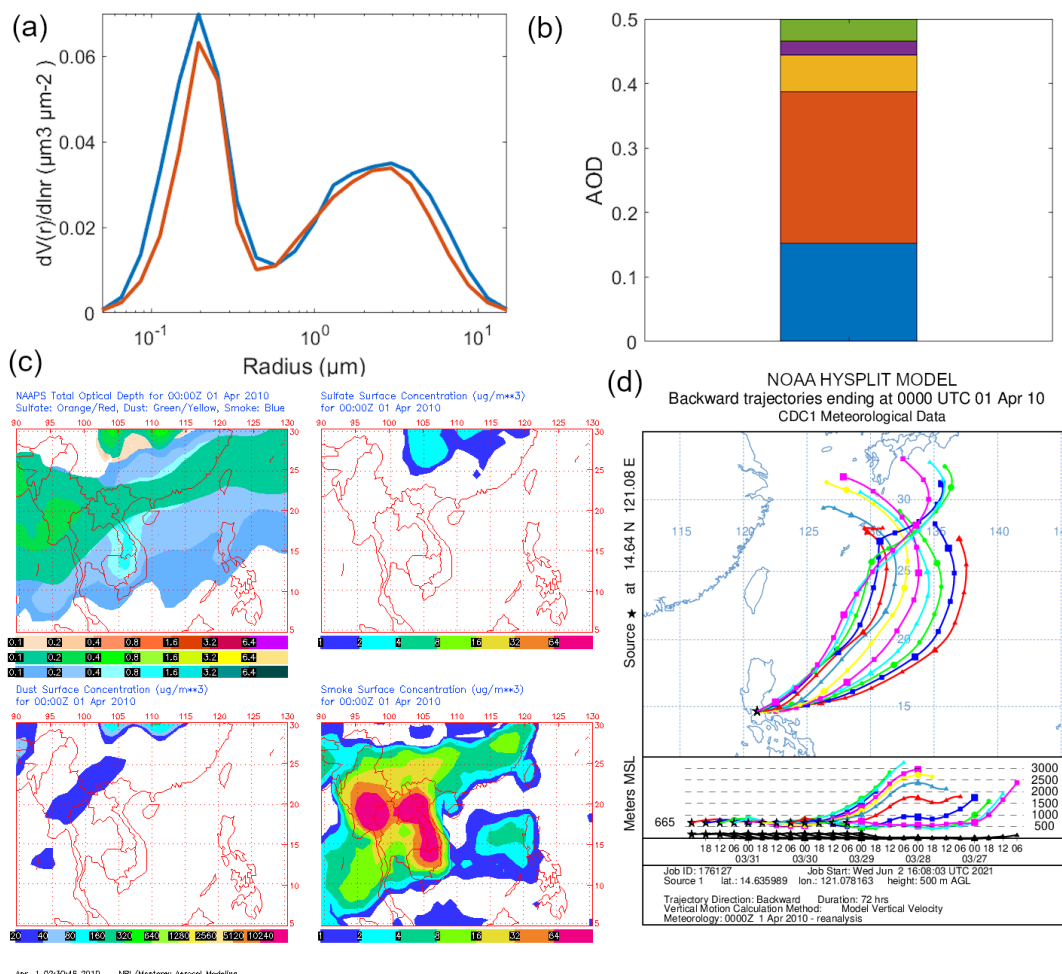
649 **3.4 Case Studies**

650 Selected case studies are used to highlight periods with the highest AOD values and strongest
651 clear sky (no rain and heavy clouds) daytime aerosol particle sources within the sampling period.
652 As such, the clusters that are associated with the selected case studies are the clusters (3-5) with
653 higher VSD magnitudes.

654

655 **3.4.1 Long Range Transport of Smoke**

656 Both cases of long-range transport of smoke discussed below have similar VSDs (Fig. 8a and 9a)
657 to the urban/industrial cluster VSD (cluster 4, Fig. 6a). Organic carbon was the dominant
658 contributor to AOD (Fig. 8b and 9b) for both long-range transport cases. The first of two events
659 occurred around 1 April 2020 with smoke presumed to come from East Asia. The VSD of this
660 specific case (Fig. 8a) is most like the urban/industrial cluster (cluster 4 in 3.3.2, Fig. 6a) because
661 of the high magnitude of its accumulated mode peak, its timing (April), and the enhanced
662 organic carbon contribution to AOD in the area (Fig. 8b). Though the absolute black carbon
663 contribution to AOD was highest here compared to the other case studies, and in general for the
664 AERONET data, it was organic carbon that was more prevalent in terms of contribution to total
665 AOD. Smoke is comprised of both soot carbon and organic carbon, amongst other constituents
666 (Reid et al., 2005).



667

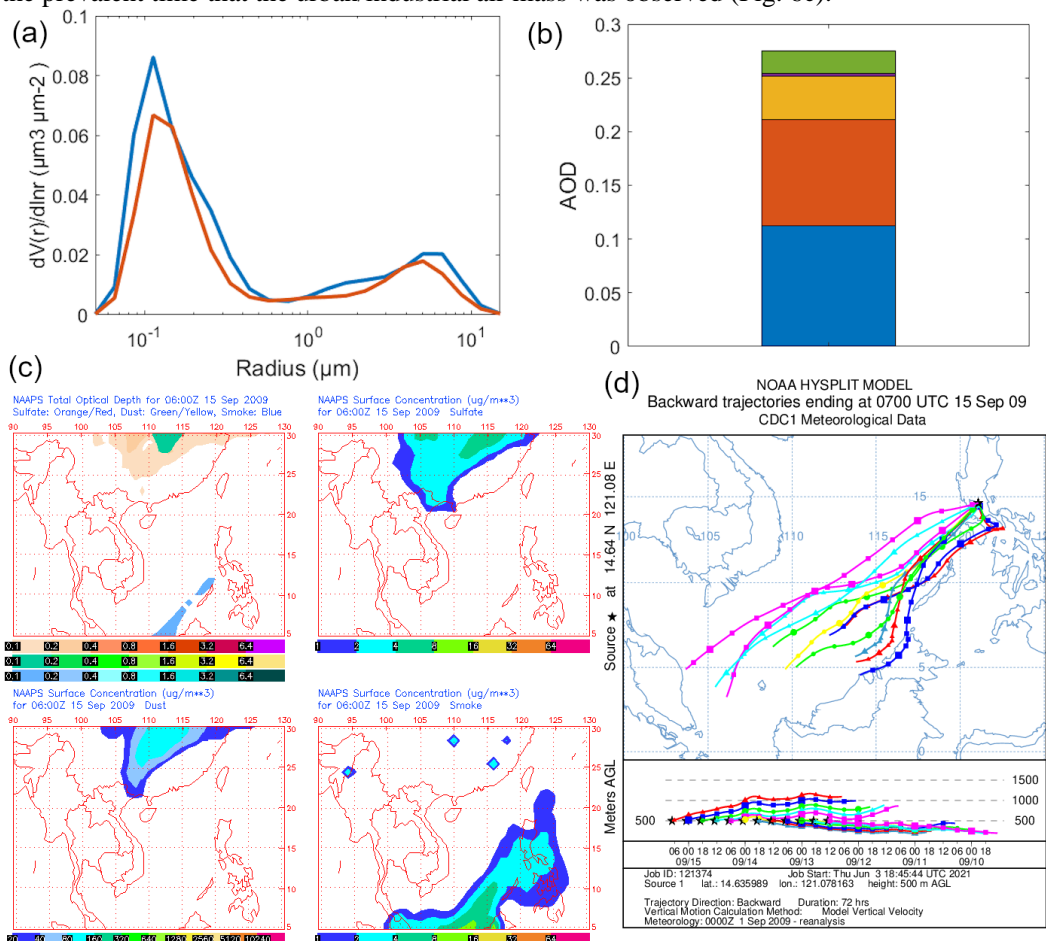
668 **Figure 8:** Case study of long-range transport (smoke – East Asia) around 1 April 2010. (a)
 669 AERONET VSDs at (blue) 00:01 and (red) 00:26 UTC, (b) MERRA-2 hourly (green: black
 670 carbon, violet: dust, yellow: sea salt, orange: organic carbon, blue: sulfate) compositional
 671 contributions to AOD closest in time to 00:01 UTC, (c) NAAPS maps of total and compositional
 672 hourly AOD (orange/red: sulfate, green/yellow: dust, blue: smoke) and sulfate, dust, and smoke
 673 surface concentrations at 00:00 UTC, and (d) HYSPLIT three-day back-trajectories arriving at
 674 Manila Observatory at 00:00 UTC.

675 The smoke contribution to AOD from NAAPS (Fig. 8c) for the first smoke case was visible in
 676 the Philippines (0.2) and seemed to come from East Asia were the smoke contribution to AOD
 677 was greater (reaching 0.8) especially in Peninsular Southeast Asia. Smoke surface concentrations
 678 were also widespread (Fig. 8c) with greatest concentrations in East Asia that reached the
 679 Western Philippines, though seemingly disconnected over the sea. There were observed biomass
 680 burning emissions in the Peninsular Southeast Asia (southern China, Burma, and Thailand) at
 681 this time (Shen et al., 2014). The direction of the air mass coming into Metro Manila was from



682 the northeast, which curved from the west in the direction of East Asia based on HYSPLIT back-
 683 trajectories (Fig. 8d).

684 The second smoke case was on 15 September 2009 with the source being Southeast Asia. The
 685 back-trajectories of this case study (Fig. 9d) are from the southwest of the Philippines, and in the
 686 direction of the Malaysia and Indonesia. NAAPS maps likewise show elevated AOD,
 687 specifically smoke contribution to AOD (Fig. 9c), as well as enhanced smoke surface
 688 contributions in the area around Metro Manila for this second smoke case study. The observed
 689 AOD and smoke surface concentration increased specifically from the southwest of the
 690 Philippines in the same direction of the back-trajectories. There were fires in the lowland (peat)
 691 forests of Borneo around this time (NASA, 2009). MERRA-2 AOD contributions for this case
 692 were greatest due to organic carbon as well as sulfate (Fig. 9b), and the absolute black carbon
 693 contributions were greatest compared to other cases. The VSD of this smoke case from Southeast
 694 Asia (Fig. 9a) resembled that from long-range transported smoke from East Asia (Fig. 8a) and
 695 the urban/industrial air mass (cluster 4, Fig. 6a). This case occurred in the afternoon, which was
 696 the prevalent time that the urban/industrial air mass was observed (Fig. 6c).





698 **Figure 9:** Case study of long-range transport (smoke – Southeast Asia) around 15 September
699 2009. (a) AERONET VSDs at (blue) 07:27 and (red) 07:52 UTC, (b) MERRA-2 hourly (green:
700 black carbon, violet: dust, yellow: sea salt, orange: organic carbon, blue: sulfate) compositional
701 contributions to AOD closest in time to 07:27 UTC, (c) NAAPS maps of total and compositional
702 hourly AOD (orange/red: sulfate, green/yellow: dust, blue: smoke) and sulfate, dust, and smoke
703 surface concentrations at 06:00 UTC, and (d) HYSPLIT three-day back-trajectories arriving at
704 Manila Observatory at 07:00 UTC.

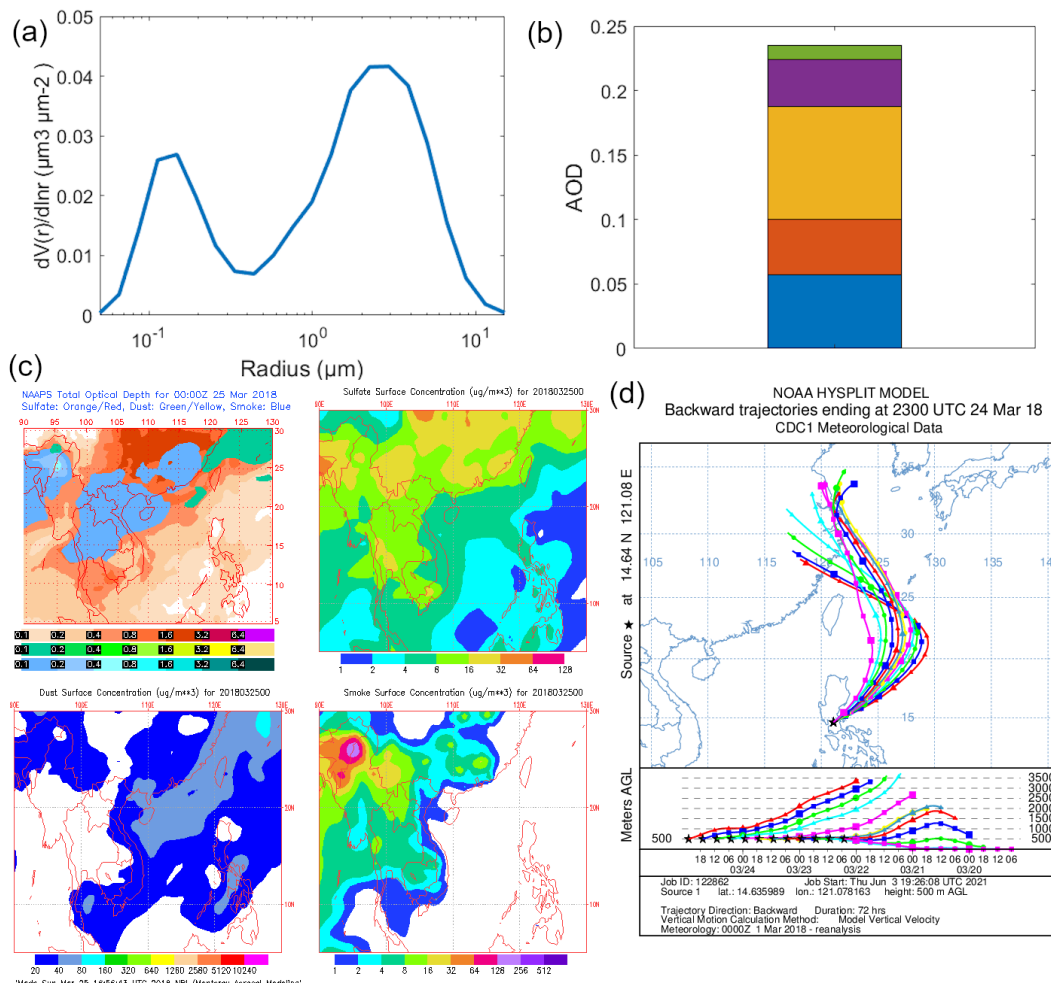
705

706 3.4.2 Long Range Transport of Dust

707 The VSD of this specific case on 24 March 2018 (Fig. 10a) was most similar to the mixed
708 polluted cluster (cluster 3), which had a mixed size distribution but a more dominant coarse
709 contribution. This is consistent with the most dominant contribution to AOD in the area, which
710 was sea salt and dust (Fig. 10b). The back-trajectories were from East Asia around the same
711 latitude as Taiwan (Fig. 10d). That area, at that time, had increased AOD in general from sulfate
712 and dust (Fig. 10c). The dust and sulfate seemed to have been transported to Metro Manila from
713 East Asia based on the NAAPS sulfate and dust surface concentrations (Fig. 10c).



714



715

716

717

718

719

720

721

722

723

724

725

726

727

728

729

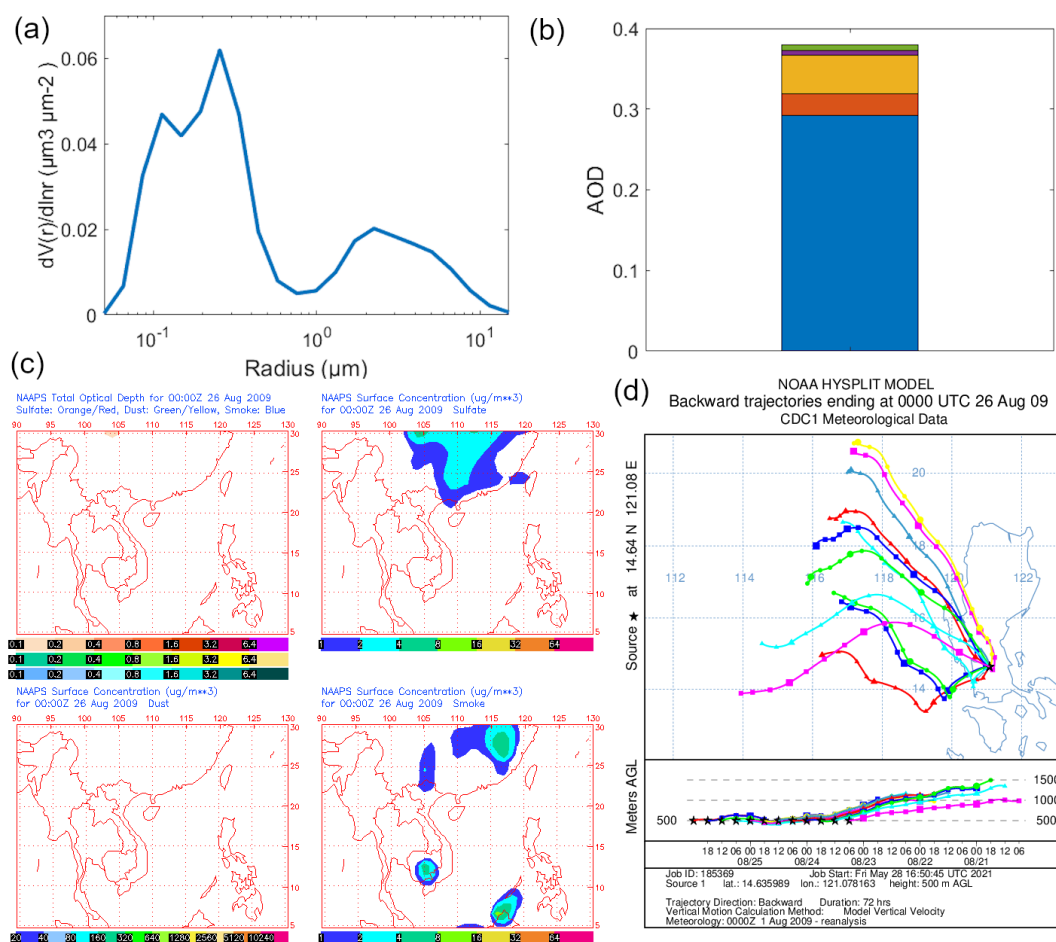
Figure 10: Case study of long-range transport (dust) around 24-25 March 2009. (a) AERONET VSD at (blue) 23:23 UTC, (b) MERRA-2 hourly (green: black carbon, violet: dust, yellow: sea salt, orange: organic carbon, blue: sulfate) compositional contributions to AOD closest in time to 23:23 UTC, (c) NAAPS maps of total and compositional hourly AOD (orange/red: sulfate, green/yellow: dust, blue: smoke) and sulfate, dust, and smoke surface concentrations at 00:00 UTC on March 25, and (d) HYSPLIT three-day back-trajectories arriving at Manila Observatory at 23:00 UTC.

3.5 Cloud Processing

Sulfate dominated the AOD (Fig. 11b) for this case on 26 August 2009 in the area around Metro Manila. This along with its VSD exhibiting a second peak (Fig. 11a) in the accumulation mode make it very similar to the cloud processing cluster (cluster 5). Sulfate has been known to be enhanced through chemical productions in clouds and is used as a signature for cloud processing (Barth et al., 2000; Ervens et al., 2018). Aqueous production of sulfate is significant in areas with



730 sources and clouds (Barth et al., 2000), and this case study has both. Aside from the high sulfate
 731 contribution to AOD, the cloud fraction is very high (~100%) in the area of the back-trajectories
 732 (Aqua/MODIS, Terra/MODIS, Fig. S2). Interestingly, there is no regional AOD elevation
 733 observed in the NAAPS maps (Fig. 11c) for this time. There are increased surface smoke and
 734 sulfate levels in East Asia as well as southwest of the Philippines, and though the back-
 735 trajectories (Fig. 11d) do show a northeastward direction, they do not reach far enough into
 736 mainland East Asia. It is possible that even while there are known regional sources of sulfate in
 737 Southeast Asia (Smith et al., 2011; Li et al., 2017), this case could be local to the Philippines.
 738 There is in fact a large power plant northwest of Metro Manila (Jamora et al., 2020).
 739



740 Aug 25 08:38:20 2009 NR/Monterey Aerosol Modeling
 741 **Figure 11:** Case study of cloud processing on 26 August 2009. (a) AERONET VSDs at 00:18
 742 UTC, (b) MERRA-2 hourly (green: black carbon, violet: dust, yellow: sea salt, orange: organic
 743 carbon, blue: sulfate) compositional contributions to AOD closest in time to 00:18 UTC, (c)
 744 NAAPS maps of total and compositional hourly AOD and contributions and smoke surface

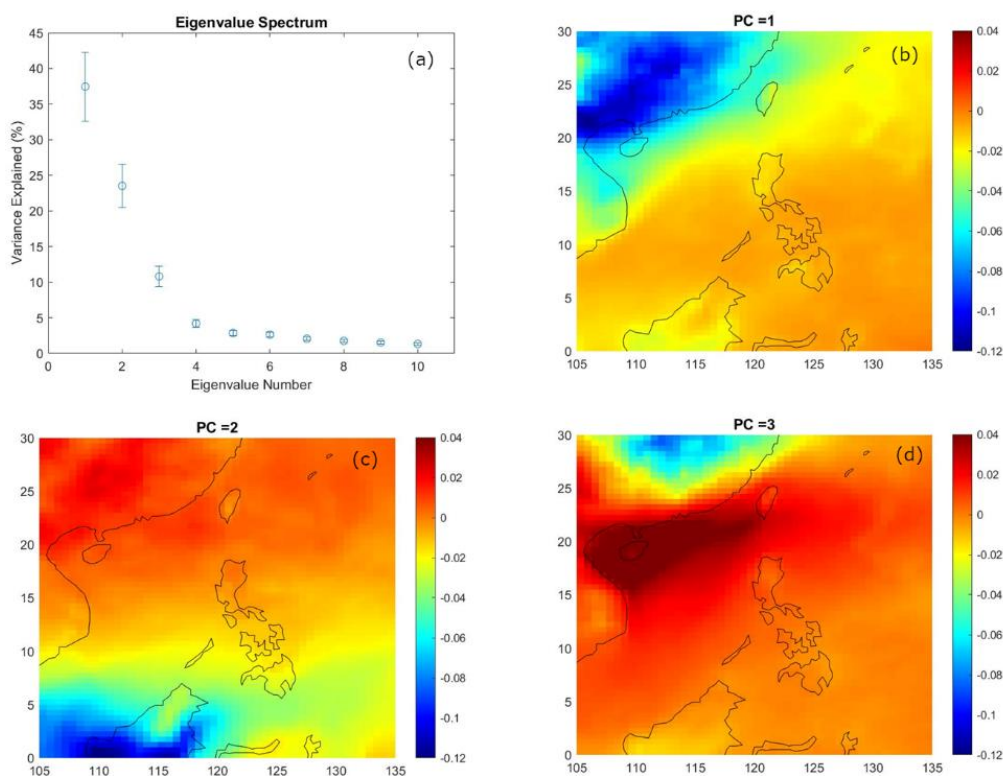


745 concentrations at 00:00 UTC, and (d) HYSPLIT three-day back-trajectories arriving at Manila
 746 Observatory at 00:00 UTC.

747

748 **3.6 EOF Analysis of AOD in Southeast Asia**

749 To contextualize the analysis of aerosol particle masses in Metro Manila, major regional sources
 750 of aerosol particles in Southeast Asia were identified based on the dominant principal
 751 components from EOF analysis of AOD. Three principal components (PC, Fig. 12) explained
 752 most of the data variance (73.77%) (Fig. 12a) and were all well-separated from each other and
 753 are therefore most probably the major distinct aerosol particle sources in the region. They will
 754 be the focus of the subsequent discussion.



755

756 **Figure 12:** Results of the singular value decomposition. (a) Eigenvalue spectrum of the first ten
 757 eigenvalues, (b-d) maps of the coefficients of regression AOD anomalies onto the first three
 758 principal components.

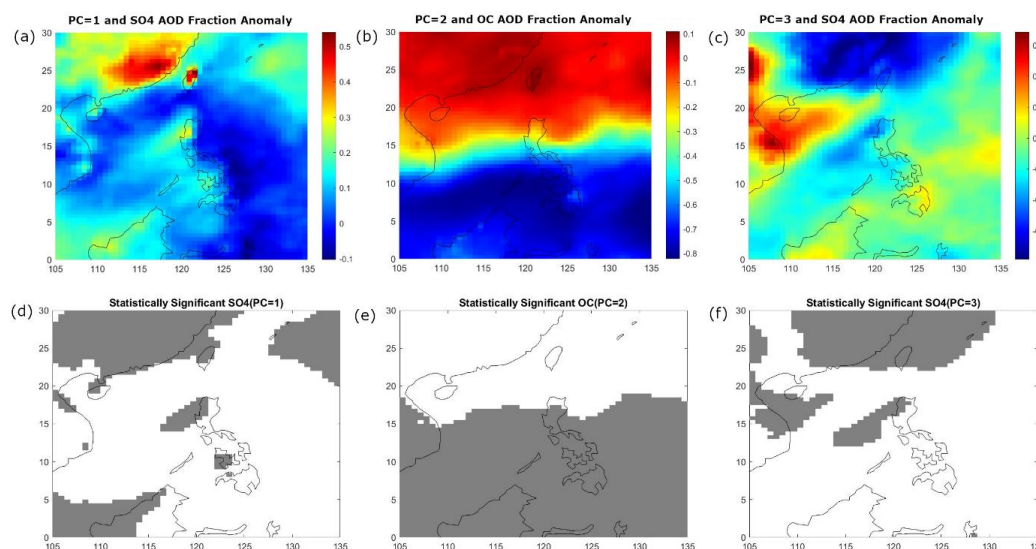
759 The first PC explains 37.46% of the data variance (Fig. 12a) and, based on the map of the
 760 regression coefficients (Fig. 12b), separates mainland East Asia from the Philippines and
 761 Indonesia. East Asia is a globally recognized source for high AOD (Li et al., 2013), and its
 762 contribution to particles in Southeast Asia possibly corresponds to the first PC. The second PC
 763 explains 25.51% of the data variance (Fig. 12a) and separates the southern Southeast Asia from
 764 northern Southeast Asia at around 15°N (Fig. 12c). Southern Southeast Asia is a known regional



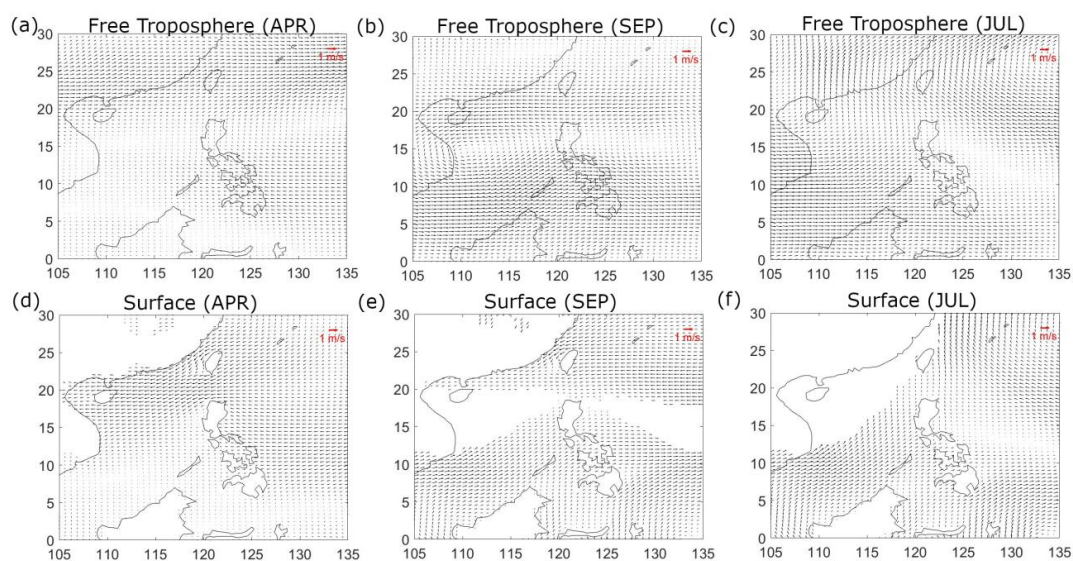
765 source of aerosol particles due to biomass burning (Cohen et al., 2017) and could be associated
 766 with the second PC. The third PC explains 10.80% of the data variance (Fig. 12a) and separates
 767 northern East Asia from southern East Asia mainland and the rest of Southeast Asia (Fig. 12d).

768 To gain confidence in the association of the PCs with their sources, we present correlation maps
 769 between the first three PCs to the fractional contributions of sulfate and organic carbon to AOD
 770 for the entire dataset.

771 The correlation maps of the first PC and the sulfate contribution to AOD (Fig. 13a and 13d)
 772 show high and statistically significant correlations (gray areas) in mainland East Asia and
 773 Taiwan, parts of western Philippines and Borneo, which are the probable sulfate sources. Clues
 774 from the mean monthly wind vector maps in April (Fig. 14a and 14d) and mean monthly AOD in
 775 either March or April (Fig. S3c or S3e) most resembling the features of regression map of the
 776 first PC (Fig. 12b) and the PC time series peaking in March (Fig. S4) together suggest that the
 777 first PC may be associated with air masses that are present around March or April. Emissions
 778 sources and meteorology that are dominant during the peak dates in the PC time series offer
 779 clues to the attribution of each PC. The Southeast Asia region and the Philippines is influenced
 780 by the monsoon systems (Coronas, 1920; Matsumoto et al., 2020) and February to March is the
 781 time when the winds are transitioning from the northeasterly to easterly. The first PC could be
 782 affected by the easterly winds, which are dominant around March when its PC values peaked.
 783 The higher-level winds (free troposphere) (Fig. 14a) in April are from the west in mainland East
 784 Asia and are from the east in the Philippines and it is possible that the different wind regimes are
 785 distinguishing the sulfate sources in East Asia and the Philippines and beyond. Sulfate is a
 786 known product of industry in East Asia (Smith et al., 2011; Li et al., 2017) while the West Luzon
 787 and West Visayas islands have large power plants (Jamora et al., 2020).



788 **Figure 13:** Correlation coefficients of principal components with (a/c) sulfate AOD fraction and
 789 (b) organic carbon AOD fraction. Statistically significant (90%, d-f) areas are shaded gray.
 790



791

792

793

Figure 14: Monthly averaged winds for (a & d) April, (b & e) September, and (c & f) July from MERRA-2 at (725 hPa, a-c) the free troposphere approximate and at (1000 hPa, d-f) the surface.

794

795

796

797

798

799

800

801

802

803

804

805

806

807

808

809

810

811

812

813

The correlation maps of the second PC and the OC contribution to AOD (Fig. 13b and 13e) show high and statistically significant correlations from 0°N to 15°N. The large magnitude of the correlation coefficient (gray areas in Fig. 13b) stands out in the southern Southeast Asia and is the potential OC source. In this case, it is known that Indonesia is a major source of biomass burning during its fire season (Glover and Jessup, 1998), and thus the local significance established in the southern Southeast Asia is most likely due to the Indonesia biomass burning source. The burning season in Indonesia is from August to October, and that is the same time when the AOD values peak in the area (Fig. S3h, S3i, and S3j), as well as the peak of the second PC in the time series (Fig. S4). Winds are usually from the southwest and west due to the southwest monsoon from September to October, when the second PC peaked, and thus the second PC may be related to the southwest monsoon. During the same time the surface and free troposphere mean monthly winds (Fig. 14b and 14e) are from the southwest (in the general direction of Indonesia) towards the south portion of Southeast Asia and thus corroborate the observation that the second PC may be highlighting the regional effect of the Indonesia forest fires. Of interest is the line of separation of the northern and southern Southeast Asia in the principal component that is within the area of the monsoon trough (Wang et al., 2007). This line is also evident in the surface and the free troposphere maps where the southwest winds from the area of Indonesia meet the easterlies in north Southeast Asia (Fig. 14b and 14e) and which thus appears to be limiting the dispersion of the biomass burning emissions to southern Southeast Asia.

814

815

816

817

818

The third PC was also well correlated to the sulfate AOD fraction though, compared to the first PC correlation maps, there were distinctions between the northern and southern East Asia regions (Fig. 13c and 13f). The local Philippine source still came out in the correlation maps as a significant source. It was not clear from the PC time series (Fig. S4), which showed peaks in the third PC in February, how the dates were related to the PC profile. The free troposphere winds in



819 July (Fig. 14c), as well as the AOD monthly mean map in July (Fig. 14c), however, showed
820 more similarities to the third PC regression map. Both showed a delineation between the
821 northern East Asia and southern East Asia (including Hong Kong) features. Mean winds (Fig.
822 14c) in the free troposphere are from the west, due to the southwest monsoon, in the area around
823 the Philippines, and they were from the northeast in north Southeast Asia. The interface of the
824 winds is within the approximate location of the monsoon trough in July (Wang et al., 2007), and
825 it is thus possible that the monsoon trough is causing the separation of the sulfate sources. This
826 could be investigated further. The monsoon trough has been noted to scavenge aerosol particles
827 from southern Southeast Asia (Reid et al., 2013). It is evident from the analysis that meteorology
828 affects the transport and processing of aerosol particles in region which along with local sources
829 contribute to the aerosol composition in Southeast Asia (Cruz et al., 2019; AzadiAghdam et al.,
830 2019; Braun et al., 2020; Hilario et al., 2020b; Hilario et al., 2022).

831

832 **4. Conclusion**

833 Metro Manila has both urban and industrial local sources known to contribute to the dominance
834 of fine mode particles in its air (Cruz et al., 2019). Ten years of AERONET data in Manila
835 Observatory suggest that aerosol particles in Metro Manila were mixed in size but with a
836 prevalent fine mode fraction (>50% FMF) throughout the year. Background clean marine aerosol
837 particles (58% of the time) and fine polluted aerosol particles (20% of the time) were the most
838 dominant clear sky day sources impacting the atmospheric column over Metro Manila based on
839 cluster analysis of volume size distributions. The proximity of Metro Manila to the sea both in
840 the east and west along with local sources, transportation being the most prominent, contribute to
841 the prevalence of the marine and fine particles. The prevalence of marine particles could explain
842 the relatively small AOD values in Metro Manila compared to other Southeast Asian megacities
843 (Reid et al., 2013).

844 Regional sources and meteorology also impact monthly aerosol optical depth trends in Metro
845 Manila from EOF analysis. Biomass burning from Borneo and Sumatra emerged in the study as
846 the second most prevalent regional anthropogenic aerosol particle source in Southeast Asia.
847 Though the monsoon trough limits the dispersion of aerosol particles throughout the entire
848 Southeast Asia, biomass burning emissions impact southern Southeast Asia including Metro
849 Manila during the southwest monsoon (July to September). The monsoon winds facilitate the
850 transport of fine particles during the peak burning season in Borneo and Sumatra (August-
851 September). This is experienced in Metro Manila as higher than usual aerosol particle loadings
852 during the same period. Climatologically, August is also when aerosol optical depth peaked over
853 Metro Manila, concurrent with greatest fine mode fractions that were relatively absorbing and
854 non-hygroscopic possibly due to increased organic and elemental carbon fractional contributions.
855 Though not as strong a source as the Borneo and Sumatra case, the peninsular Southeast Asia
856 burning season (March-April) also contributed to extreme aerosol particle concentrations over
857 Metro Manila.

858 High aerosol particle loadings due to transported dust, probably from East Asia, were observed
859 in Metro Manila during the transition period between the southwest and northeast monsoons and
860 during the northeast monsoon (December to February). These extreme events are transient
861 because the lowest median aerosol particle loadings of the year were observed during the
862 northeast monsoon when annual wind speeds were highest. Particles then were observed to be



863 largest in diameter, with the greatest coarse fraction contribution and most hygroscopicity,
864 compared to other months of the year. This is probably due to constituents other than soot,
865 especially aged dust (Kim and Park, 2012; Geng et al., 2014) and sea salt which the northeast
866 winds appear to be bringing in from the general direction of the Luzon Island and the Philippine
867 Sea (West Pacific Ocean).

868 Cloud processing is one of the cases that were linked to very high aerosol particle loading in
869 Metro Manila. This is associated with sulfate sources, which appear more localized in nature
870 because of a power plant nearby. This sulfate source seems to be distinct from the industrial
871 sulfate air mass from East Asia, which is the most dominant regional aerosol particle source in
872 Southeast Asia (Li et al., 2013). Winds appear to limit the mixing of this notable East Asia air
873 mass with local industrial sources in the region including the Philippines and Indonesia.

874 The formation of cloud systems in Southeast Asia is complex due to intersecting large- and
875 small-scale mechanisms. Additionally, the interaction of particles and clouds in Southeast Asia is
876 not yet well understood. In Metro Manila, both topography and meteorology affect aerosol
877 particle distribution (Cruz et al., 2023). This baseline study on the aerosol particle characteristics
878 in Metro Manila and in regional Southeast Asia shows how meteorology impacts varied aerosol
879 particle sources (e.g., sulfate, elemental carbon, and organic carbon) and their distribution in the
880 region. This can help in mitigating aerosol particle sources in the region and in the deepening of
881 the understanding of the relationship of aerosol particles, meteorology, and clouds.
882

883 **Data availability**

884 Aerosol Robotic Network (AERONET) (2020), Version 3 Direct Sun Algorithm, Site: Manila
885 Observatory, Philippines, Accessed: [28 September 2020], [https://aeronet.gsfc.nasa.gov/cgi-](https://aeronet.gsfc.nasa.gov/cgi-bin/webtool_aod_v3?stage=3®ion=Asia&state=Philippines&site=Manila_Observatory&place_code=10&if_polarized=0)
886 [bin/webtool_aod_v3?stage=3®ion=Asia&state=Philippines&site=Manila_Observatory&place](https://aeronet.gsfc.nasa.gov/cgi-bin/webtool_aod_v3?stage=3®ion=Asia&state=Philippines&site=Manila_Observatory&place_code=10&if_polarized=0)
887 [_code=10&if_polarized=0](https://aeronet.gsfc.nasa.gov/cgi-bin/webtool_aod_v3?stage=3®ion=Asia&state=Philippines&site=Manila_Observatory&place_code=10&if_polarized=0)

888 Aerosol Robotic Network (AERONET) (2020), Version 3 Direct Sun and Inversion Algorithm,
889 Site: Manila Observatory, Philippines, Accessed: [28 September 2020],
890 [https://aeronet.gsfc.nasa.gov/cgi-](https://aeronet.gsfc.nasa.gov/cgi-bin/webtool_inv_v3?stage=3®ion=Asia&state=Philippines&site=Manila_Observatory&place_code=10&if_polarized=0)
891 [bin/webtool_inv_v3?stage=3®ion=Asia&state=Philippines&site=Manila_Observatory&place](https://aeronet.gsfc.nasa.gov/cgi-bin/webtool_inv_v3?stage=3®ion=Asia&state=Philippines&site=Manila_Observatory&place_code=10&if_polarized=0)
892 [_code=10&if_polarized=0](https://aeronet.gsfc.nasa.gov/cgi-bin/webtool_inv_v3?stage=3®ion=Asia&state=Philippines&site=Manila_Observatory&place_code=10&if_polarized=0)

893 Multi-angle Imaging SpectroRadiometer (MISR) Jet Propulsion Laboratory (2018), Level 3
894 Component Global Aerosol product in netCDF format covering a month V004, Accessed: [22
895 November 2021], <https://search.earthdata.nasa.gov/>

896 Global Modeling and Assimilation Office (GMAO) (2015), MERRA-2 inst3_3d_asm_Np: 3d,3-
897 Hourly,Instantaneous,Pressure-Level,Assimilation,Assimilated Meteorological Fields V5.12.4,
898 Greenbelt, MD, USA, Goddard Earth Sciences Data and Information Services Center (GES
899 DISC), Accessed: [10 March 2021], <https://doi.org/10.5067/QBZ6MG944HW0>

900 Global Modeling and Assimilation Office (GMAO) (2015), MERRA-2 tavg1_2d_flux_Nx: 2d,1-
901 Hourly,Time-Averaged,Single-Level,Assimilation,Surface Flux Diagnostics V5.12.4, Greenbelt,



- 902 MD, USA, Goddard Earth Sciences Data and Information Services Center (GES DISC),
903 Accessed: [**10 March 2021**], <https://doi.org/10.5067/7MCPBJ41Y0K6>
- 904 Global Modeling and Assimilation Office (GMAO) (2015), MERRA-2 tavg1_2d_csp_Nx: 2d,1-
905 Hourly,Time-averaged,Single-Level,Assimilation,COSP Satellite Simulator V5.12.4, Greenbelt,
906 MD, USA, Goddard Earth Sciences Data and Information Services Center (GES DISC),
907 Accessed: [**13 July 2021**], <https://doi.org/10.5067/H0VVAD8F6MX5>
- 908 Nguyen, P., E.J. Shearer, H. Tran, M. Ombadi, N. Hayatbini, T. Palacios, P. Huynh, G.
909 Updegraff, K. Hsu, B. Kuligowski, W.S. Logan, and S. Sorooshian, The CHRS Data Portal, an
910 easily accessible public repository for PERSIANN global satellite precipitation data, Nature
911 Scientific Data, Vol. 6, Article 180296, 2019, Accessed: [**11 March 2021**],
912 <https://doi.org/10.1038/sdata.2018.296>

913

914 **Author contributions**

915 GRL and AS designed the experiment. NL, SNU, GRL, GFG, HJO, JBS, and MTC, carried out
916 various aspects of the data collection. GRL, AS, JBS, MOC, MRH, and CC conducted analysis
917 and interpretation of the data. GRL prepared the manuscript draft with contributions from the
918 coauthors. AFA, LDG, MRH, GRL, and AS reviewed and edited the manuscript. AS led the
919 management and funding acquisition. All authors approved the final version of the manuscript.

920

921 **Competing interests**

922 We declare that Armin Sorooshian is a member of the editorial board of Atmospheric Chemistry
923 and Physics. The peer-review process was guided by an independent editor, and the authors have
924 also no other competing interests to declare.

925

926 **Acknowledgements**

927 The authors acknowledge support from NASA grant 80NSSC18K0148 in support of the NASA
928 CAMP²Ex project, in addition to ONR grant N00014-21-1-2115. We acknowledge the US Naval
929 Research Laboratory for providing the AERONET instrument. We acknowledge the use of
930 imagery from the NASA Worldview application (<https://worldview.earthdata.nasa.gov>), part of
931 the NASA Earth Observing System Data and Information System (EOSDIS).

932

933 **References:**

- 934 AERONET Inversion Products (Version 3):
935 https://aeronet.gsfc.nasa.gov/new_web/Documents/Inversion_products_for_V3.pdf, access: June
936 25, 2021, 2019.
- 937 Alas, H. D., Müller, T., Birmili, W., Kecorius, S., Cambaliza, M. O., Simpas, J. B. B., Cayetano,
938 M., Weinhold, K., Vallar, E., and Galvez, M. C.: Spatial characterization of black carbon mass
939 concentration in the atmosphere of a southeast asian megacity: an air quality case study for
940 Metro Manila, Philippines, Aerosol Air Qual. Res., 18, 2301-2317,
941 <https://doi.org/10.4209/aaqr.2017.08.0281>, 2018.



- 942 Aldhaif, A. M., Lopez, D. H., Dadashazar, H., and Sorooshian, A.: Sources, frequency, and
943 chemical nature of dust events impacting the United States East Coast, *Atmos. Environ.*, 231,
944 117456, <https://doi.org/10.1016/j.atmosenv.2020.117456>, 2020.
- 945 Aldhaif, A. M., Lopez, D. H., Dadashazar, H., Painemal, D., Peters, A. J., and Sorooshian, A.:
946 An Aerosol Climatology and Implications for Clouds at a Remote Marine Site: Case Study Over
947 Bermuda, *J. Geophys. Res.- Atmos.*, 126, e2020JD034038,
948 <https://doi.org/10.1029/2020JD034038>, 2021.
- 949 Alizadeh-Choobari, O., and Gharaylou, M.: Aerosol impacts on radiative and microphysical
950 properties of clouds and precipitation formation, *Atmos. Res.*, 185, 53-64,
951 <https://doi.org/10.1016/j.atmosres.2016.10.021>, 2017.
- 952 Andrews, E., Ogren, J. A., Kinne, S., and Samset, B.: Comparison of AOD, AAOD and column
953 single scattering albedo from AERONET retrievals and in situ profiling measurements, *Atmos.*
954 *Chem. Phys.*, 17, 6041-6072, <https://doi.org/10.5194/acp-17-6041-2017>, 2017.
- 955 Ångström, A.: On the atmospheric transmission of sun radiation and on dust in the air,
956 *Geografiska Annaler*, 11, 156-166, 1929.
- 957 Arthur, D., and Vassilvitskii, S.: k-means++: The advantages of careful seeding, Stanford, 2006.
- 958 AzadiAghdam, M., Braun, R. A., Edwards, E.-L., Bañaga, P. A., Cruz, M. T., Betito, G.,
959 Cambaliza, M. O., Dadashazar, H., Lorenzo, G. R., and Ma, L.: On the nature of sea salt aerosol
960 at a coastal megacity: Insights from Manila, Philippines in Southeast Asia, *Atmos. Environ.*, 216,
961 116922, <https://doi.org/10.1016/j.atmosenv.2019.116922>, 2019.
- 962 Bañares, E. N., Narisma, G. T. T., Simpas, J. B. B., Cruz, F. A. T., Lorenzo, G. R. H.,
963 Cambaliza, M. O. L., and Coronel, R. C.: Seasonal and diurnal variations of observed convective
964 rain events in metro Manila, Philippines, *Atmos. Res.*, 105646,
965 <https://doi.org/10.1016/j.atmosres.2021.105646>, 2021.
- 966 Barth, M., Rasch, P., Kiehl, J., Benkovitz, C., and Schwartz, S.: Sulfur chemistry in the National
967 Center for Atmospheric Research Community Climate Model: Description, evaluation, features,
968 and sensitivity to aqueous chemistry, *J. Geophys. Res.- Atmos.*, 105, 1387-1415,
969 <https://doi.org/10.1029/1999JD900773>, 2000.
- 970 Bergstrom, R. W., Russell, P. B., and Hignett, P.: Wavelength dependence of the absorption of
971 black carbon particles: Predictions and results from the TARFOX experiment and implications
972 for the aerosol single scattering albedo, *J. Atmos. Sci.*, 59, 567-577,
973 [https://doi.org/10.1175/1520-0469\(2002\)059<0567:WDOTAO>2.0.CO;2](https://doi.org/10.1175/1520-0469(2002)059<0567:WDOTAO>2.0.CO;2), 2002.
- 974 Bergstrom, R. W., Pilewskie, P., Schmid, B., and Russell, P. B.: Estimates of the spectral aerosol
975 single scattering albedo and aerosol radiative effects during SAFARI 2000, *J. Geophys. Res.-*
976 *Atmos.*, 108, <https://doi.org/10.1029/2002JD002435>, 2003.
- 977 Bergstrom, R. W., Pilewskie, P., Russell, P. B., Redemann, J., Bond, T. C., Quinn, P. K., and
978 Sierau, B.: Spectral absorption properties of atmospheric aerosols, *Atmos. Chem. Phys.*, 7, 5937-
979 5943, <https://doi.org/10.5194/acp-7-5937-2007>, 2007.
- 980 Bi, J., Huang, J., Hu, Z., Holben, B., and Guo, Z.: Investigating the aerosol optical and radiative
981 characteristics of heavy haze episodes in Beijing during January of 2013, *J. Geophys. Res.-*
982 *Atmos.*, 119, 9884-9900, <https://doi.org/10.1002/2014JD021757>, 2014.
- 983 Björnsson, H., and Venegas, S.: A manual for EOF and SVD analyses of climatic data, CCGCR
984 Report, 97, 112-134, 1997.
- 985 Bohren, C. F., and Clothiaux, E. E.: Fundamentals of atmospheric radiation: an introduction with
986 400 problems, John Wiley & Sons, 2006.



- 987 Braun, R. A., Aghdam, M. A., Bañaga, P. A., Betito, G., Cambaliza, M. O., Cruz, M. T.,
988 Lorenzo, G. R., MacDonald, A. B., Simpas, J. B., and Stahl, C.: Long-range aerosol transport
989 and impacts on size-resolved aerosol composition in Metro Manila, Philippines, *Atmos. Chem.*
990 *Phys.*, 20, 2387–2405, <https://doi.org/10.5194/acp-20-2387-2020>, 2020.
- 991 Che, H., Xia, X., Zhu, J., Wang, H., Wang, Y., Sun, J., Zhang, X., and Shi, G.: Aerosol optical
992 properties under the condition of heavy haze over an urban site of Beijing, China, *Environ. Sci.*
993 *Pollut. R.*, 22, 1043–1053, <https://doi.org/10.1007/s11356-014-3415-5>, 2015.
- 994 Chen, Q., McGowan, S., Gouramanis, C., Fong, L., Balasubramanian, R., and Taylor, D.:
995 Rapidly rising transboundary atmospheric pollution from industrial and urban sources in
996 Southeast Asia and its implications for regional sustainable development, *Environ. Res. Lett.*, 15,
997 1040a1045, <https://doi.org/10.1088/1748-9326/abb5ce>, 2020.
- 998 Choi, M., Lim, H., Kim, J., Lee, S., Eck, T. F., Holben, B. N., Garay, M. J., Hyer, E. J., Saide, P.
999 E., and Liu, H.: Validation, comparison, and integration of GOCI, AHI, MODIS, MISR, and
1000 VIIRS aerosol optical depth over East Asia during the 2016 KORUS-AQ campaign, *Atmos.*
1001 *Meas. Tech.*, 12, 4619–4641, <https://doi.org/10.5194/amt-12-4619-2019>, 2019.
- 1002 Cohen, J. B., Lecoecur, E., and Hui Loong Ng, D.: Decadal-scale relationship between
1003 measurements of aerosols, land-use change, and fire over Southeast Asia, *Atmos. Chem. Phys.*,
1004 17, 721–743, <https://doi.org/10.5194/acp-17-721-2017>, 2017.
- 1005 Coronas, J.: *The Climate and Weather of the Philippines, 1903–1918*, by Rev. José Coronas. SJ,
1006 Chief, Meteorological Division, Weather Bureau, Manila Observatory, Manila.: Bureau of
1007 Printing, 1920.
- 1008 Crosbie, E., Sorooshian, A., Monfared, N. A., Shingler, T., and Esmaili, O.: A multi-year aerosol
1009 characterization for the greater Tehran area using satellite, surface, and modeling data,
1010 *Atmosphere*, 5, 178–197, <https://doi.org/10.3390/atmos5020178>, 2014.
- 1011 Crosbie, E., Ziemba, L. D., Shook, M. A., Robinson, C. E., Winstead, E. L., Thornhill, K. L.,
1012 Braun, R. A., MacDonald, A. B., Stahl, C., and Sorooshian, A.: Measurement report: Closure
1013 analysis of aerosol–cloud composition in tropical maritime warm convection, *Atmos. Chem.*
1014 *Phys.*, 22, 13269–13302, <https://doi.org/10.5194/acp-22-13269-2022>, 2022.
- 1015 Cruz, F., Narisma, G. T., Villafuerte II, M. Q., Chua, K. C., and Olaguera, L. M.: A
1016 climatological analysis of the southwest monsoon rainfall in the Philippines, *Atmos. Res.*, 122,
1017 609–616, <https://doi.org/10.1016/j.atmosres.2012.06.010>, 2013.
- 1018 Cruz, M. T., Bañaga, P. A., Betito, G., Braun, R. A., Stahl, C., Aghdam, M. A., Cambaliza, M.
1019 O., Dadashazar, H., Hilario, M. R., Lorenzo, G. R., Ma, L., MacDonald, A. B., Pabroa, C., Yee,
1020 J. R., Simpas, J. B., and Sorooshian, A.: Size-resolved composition and morphology of
1021 particulate matter during the southwest monsoon in Metro Manila, Philippines, *Atmos. Chem.*
1022 *Phys.*, 19, 10675–10696, <https://doi.org/10.5194/acp-19-10675-2019>, 2019.
- 1023 Cruz, M. T., Simpas, J. B., Sorooshian, A., Betito, G., Cambaliza, M. O. L., Collado, J. T.,
1024 Eloranta, E. W., Holz, R., Topacio, X. G. V., and Del Socorro, J.: Impacts of regional wind
1025 circulations on aerosol pollution and planetary boundary layer structure in Metro Manila,
1026 Philippines, *Atmos. Environ.*, 293, 119455, <https://doi.org/10.1016/j.atmosenv.2022.119455>,
1027 2023.
- 1028 Di Girolamo, L., Holz, R., Reid, J., Tanelli, S., van den Heever, S., Narsma, G., and Simpas, J.:
1029 Cloud and aerosol monsoonal processes-Philippines experiment (CAMP2Ex), NASA White
1030 Paper, 2015.
- 1031 Diner, D. J., Di Girolamo, L., and Nolin, A.: Preface to the MISR special issue, *Remote Sens.*
1032 *Environ.*, 107, 1, <https://doi.org/10.1016/j.rse.2006.11.001>, 2007.



- 1033 Dubovik, O., Holben, B., Kaufman, Y., Yamasoe, M., Smirnov, A., Tanré, D., and Slutsker, I.:
1034 Single-scattering albedo of smoke retrieved from the sky radiance and solar transmittance
1035 measured from ground, *J. Geophys. Res.- Atmos.*, 103, 31903-31923,
1036 <https://doi.org/10.1029/98JD02276>, 1998.
- 1037 Dubovik, O., and King, M. D.: A flexible inversion algorithm for retrieval of aerosol optical
1038 properties from Sun and sky radiance measurements, *J. Geophys. Res.- Atmos.*, 105, 20673-
1039 20696, <https://doi.org/10.1029/2000JD900282>, 2000.
- 1040 Dubovik, O., Holben, B., Eck, T. F., Smirnov, A., Kaufman, Y. J., King, M. D., Tanré, D., and
1041 Slutsker, I.: Variability of absorption and optical properties of key aerosol types observed in
1042 worldwide locations, *J. Atmos. Sci.*, 59, 590-608, [https://doi.org/10.1175/1520-
1043 0469\(2002\)059<0590:VOAAOP>2.0.CO;2](https://doi.org/10.1175/1520-0469(2002)059<0590:VOAAOP>2.0.CO;2), 2002.
- 1044 Eck, T., Holben, B., Reid, J., O'Neill, N., Schafer, J., Dubovik, O., Smirnov, A., Yamasoe, M.,
1045 and Artaxo, P.: High aerosol optical depth biomass burning events: A comparison of optical
1046 properties for different source regions, *Geophys. Res. Lett.*, 30,
1047 <https://doi.org/10.1029/2003GL017861>, 2003.
- 1048 Eck, T., Holben, B., Dubovik, O., Smirnov, A., Goloub, P., Chen, H., Chatenet, B., Gomes, L.,
1049 Zhang, X. Y., and Tsay, S. C.: Columnar aerosol optical properties at AERONET sites in central
1050 eastern Asia and aerosol transport to the tropical mid-Pacific, *J. Geophys. Res.- Atmos.*, 110,
1051 <https://doi.org/10.1029/2004JD005274>, 2005.
- 1052 Eck, T., Holben, B., Reid, J., Mukelabai, M., Piketh, S., Torres, O., Jethva, H., Hyer, E., Ward,
1053 D., and Dubovik, O.: A seasonal trend of single scattering albedo in southern African biomass-
1054 burning particles: Implications for satellite products and estimates of emissions for the world's
1055 largest biomass-burning source, *J. Geophys. Res.- Atmos.*, 118, 6414-6432,
1056 <https://doi.org/10.1002/jgrd.50500>, 2013.
- 1057 Eck, T. F., Holben, B., Reid, J., Dubovik, O., Smirnov, A., O'Neill, N., Slutsker, I., and Kinne, S.:
1058 Wavelength dependence of the optical depth of biomass burning, urban, and desert dust aerosols,
1059 *J. Geophys. Res.- Atmos.*, 104, 31333-31349, <https://doi.org/10.1029/1999JD900923>, 1999.
- 1060 Eck, T. F., Holben, B. N., Reid, J., Giles, D., Rivas, M., Singh, R. P., Tripathi, S., Bruegge, C.,
1061 Platnick, S., and Arnold, G.: Fog-and cloud-induced aerosol modification observed by the
1062 Aerosol Robotic Network (AERONET), *J. Geophys. Res.- Atmos.*, 117,
1063 <https://doi.org/10.1029/2011JD016839>, 2012.
- 1064 Ervens, B., Sorooshian, A., Aldhaif, A. M., Shingler, T., Crosbie, E., Ziemba, L., Campuzano-
1065 Jost, P., Jimenez, J. L., and Wisthaler, A.: Is there an aerosol signature of chemical cloud
1066 processing?, *Atmos. Chem. Phys.*, 18, 16099-16119, <https://doi.org/10.5194/acp-18-16099-2018>,
1067 2018.
- 1068 Faloona, I.: Sulfur processing in the marine atmospheric boundary layer: A review and critical
1069 assessment of modeling uncertainties, *Atmos. Environ.*, 43, 2841-2854,
1070 <https://doi.org/10.1016/j.atmosenv.2009.02.043>, 2009.
- 1071 Feingold, G.: Modeling of the first indirect effect: Analysis of measurement requirements,
1072 *Geophys. Res. Lett.*, 30, <https://doi.org/10.1029/2003GL017967>, 2003.
- 1073 Flores, J.: Climate of the Philippines, *Climates of the Northern and Eastern Asia*, 159-213, 1969.
- 1074 Formenti, P., Andreae, M. O., and Lelieveld, J.: Measurements of aerosol optical depth above
1075 3570 m asl in the North Atlantic free troposphere: results from ACE-2, *Tellus B*, 52, 678-693,
1076 <https://doi.org/10.1034/j.1600-0889.2000.00006.x>, 2000.
- 1077 Garay, M. J., Bull, M. A., Nastan, A. M., Witek, M. L., Seidel, F. C., Diner, D. J., Kahn, R. A.,
1078 Limbacher, J. A., and Kalashnikova, O. V.: Data Product Specification for the MISR Level 2



- 1079 Aerosol Product, Jet Propulsion Laboratory, California Institute of Technology. JPL D-100649.
1080 https://asdc.larc.nasa.gov/documents/misr/DPS_AEROSOL_V023.20180125.pdf, 2018.
- 1081 Gautam, R., Hsu, N. C., Eck, T. F., Holben, B. N., Janjai, S., Jantarach, T., Tsay, S.-C., and Lau,
1082 W. K.: Characterization of aerosols over the Indochina peninsula from satellite-surface
1083 observations during biomass burning pre-monsoon season, *Atmos. Environ.*, 78, 51-59,
1084 <https://doi.org/10.1016/j.atmosenv.2012.05.038>, 2013.
- 1085 Gelaro, R., McCarty, W., Suárez, M. J., Todling, R., Molod, A., Takacs, L., Randles, C. A.,
1086 Darmenov, A., Bosilovich, M. G., and Reichle, R.: The modern-era retrospective analysis for
1087 research and applications, version 2 (MERRA-2), *J. Climate*, 30, 5419-5454,
1088 <https://doi.org/10.1175/JCLI-D-16-0758.1>, 2017.
- 1089 Geng, H., Hwang, H., Liu, X., Dong, S., and Ro, C.-U.: Investigation of aged aerosols in size-
1090 resolved Asian dust storm particles transported from Beijing, China, to Incheon, Korea, using
1091 low-Z particle EPMA, *Atmos. Chem. Phys.*, 14, 3307-3323, <https://doi.org/10.5194/acp-14-3307-2014>, 2014.
- 1093 Giles, D. M., Holben, B. N., Eck, T. F., Sinyuk, A., Smirnov, A., Slutsker, I., Dickerson, R.,
1094 Thompson, A., and Schafer, J.: An analysis of AERONET aerosol absorption properties and
1095 classifications representative of aerosol source regions, *J. Geophys. Res.- Atmos.*, 117,
1096 <https://doi.org/10.1029/2012JD018127>, 2012.
- 1097 Giles, D. M., Sinyuk, A., Sorokin, M. G., Schafer, J. S., Smirnov, A., Slutsker, I., Eck, T. F.,
1098 Holben, B. N., Lewis, J. R., and Campbell, J. R.: Advancements in the Aerosol Robotic Network
1099 (AERONET) Version 3 database—automated near-real-time quality control algorithm with
1100 improved cloud screening for Sun photometer aerosol optical depth (AOD) measurements,
1101 *Atmos. Meas. Tech.*, 12, 169-209, <https://doi.org/10.5194/amt-12-169-2019>, 2019.
- 1102 Glover, D., and Jessup, T.: The Indonesian fires and haze of 1997: the economic toll, *Economy
1103 and Environment Program for SE Asia (EEPSEA) Singapore and the World Wildlife Fund
1104 (WWF) Indonesia*, Jakarta, 1998.
- 1105 Guyon, P., Boucher, O., Graham, B., Beck, J., Mayol-Bracero, O. L., Roberts, G. C., Maenhaut,
1106 W., Artaxo, P., and Andreae, M. O.: Refractive index of aerosol particles over the Amazon
1107 tropical forest during LBA-EUSTACH 1999, *J. Aerosol Sci.*, 34, 883-907,
1108 [https://doi.org/10.1016/S0021-8502\(03\)00052-1](https://doi.org/10.1016/S0021-8502(03)00052-1), 2003.
- 1109 Hartley, W. S., and Hobbs, P. V.: An aerosol model and aerosol-induced changes in the clear-sky
1110 albedo off the east coast of the United States, *J. Geophys. Res.- Atmos.*, 106, 9733-9748,
1111 <https://doi.org/10.1029/2001JD900025>, 2001.
- 1112 Haywood, J., and Boucher, O.: Estimates of the direct and indirect radiative forcing due to
1113 tropospheric aerosols: A review, *Rev. Geophys.*, 38, 513-543,
1114 <https://doi.org/10.1029/1999RG000078>, 2000.
- 1115 Herber, A., Thomason, L. W., Gernandt, H., Leiterer, U., Nagel, D., Schulz, K. H., Kaptur, J.,
1116 Albrecht, T., and Notholt, J.: Continuous day and night aerosol optical depth observations in the
1117 Arctic between 1991 and 1999, *J. Geophys. Res.- Atmos.*, 107, AAC 6-1-AAC 6-13,
1118 <https://doi.org/10.1029/2001JD000536>, 2002.
- 1119 Hilario, M. R. A., Cruz, M. T., Bañaga, P. A., Betito, G., Braun, R. A., Stahl, C., Cambaliza, M.
1120 O., Lorenzo, G. R., MacDonald, A. B., AzadiAghdam, M., Pabroa, P. C., Yee, J. R., Simpas, J.
1121 B., and Sorooshian, A.: Characterizing weekly cycles of particulate matter in a coastal megacity:
1122 The importance of a seasonal, size-resolved, and chemically-speciated analysis, *J. Geophys.
1123 Res.- Atmos.*, 125, e2020JD032614, <https://doi.org/10.1029/2020JD032614>, 2020a.



- 1124 Hilario, M. R. A., Cruz, M. T., Cambaliza, M. O. L., Reid, J. S., Xian, P., Simpas, J. B.,
1125 Lagrosas, N. D., Uy, S. N. Y., Cliff, S., and Zhao, Y.: Investigating size-segregated sources of
1126 elemental composition of particulate matter in the South China Sea during the 2011 Vasco
1127 cruise, *Atmos. Chem. Phys.*, 20, 1255-1276, <https://doi.org/10.5194/acp-20-1255-2020>, 2020b.
1128 Hilario, M. R. A., Crosbie, E., Shook, M., Reid, J. S., Cambaliza, M. O. L., Simpas, J. B. B.,
1129 Ziemba, L., DiGangi, J. P., Diskin, G. S., and Nguyen, P.: Measurement report: Long-range
1130 transport patterns into the tropical northwest Pacific during the CAMP 2 Ex aircraft campaign:
1131 chemical composition, size distributions, and the impact of convection, *Atmos. Chem. Phys.*, 21,
1132 3777-3802, <https://doi.org/10.5194/acp-21-3777-2021>, 2021a.
1133 Hilario, M. R. A., Olaguera, L. M., Narisma, G. T., and Matsumoto, J.: Diurnal characteristics of
1134 summer precipitation over Luzon Island, Philippines, *Asia-Pacific Journal of Atmospheric
1135 Sciences*, 57, 573-585, <https://doi.org/10.1007/s13143-020-00214-1>, 2021b.
1136 Hilario, M. R. A., Bañaga, P. A., Betito, G., Braun, R. A., Cambaliza, M. O., Cruz, M. T.,
1137 Lorenzo, G. R., MacDonald, A. B., Pabroa, P. C., and Simpas, J. B.: Stubborn aerosol: why
1138 particulate mass concentrations do not drop during the wet season in Metro Manila, Philippines,
1139 *Environmental Science: Atmospheres*, 2, 1428-1437, <https://doi.org/10.1039/D2EA00073C>,
1140 2022.
1141 Hogan, T. F., Liu, M., Ridout, J. A., Peng, M. S., Whitcomb, T. R., Ruston, B. C., Reynolds, C.
1142 A., Eckermann, S. D., Moskaitis, J. R., and Baker, N. L.: The navy global environmental model,
1143 *Oceanography*, 27, 116-125, <https://doi.org/10.5670/oceanog.2014.73>, 2014.
1144 Holben, B. N., Eck, T. F., Slutsker, I. a., Tanre, D., Buis, J., Setzer, A., Vermote, E., Reagan, J.
1145 A., Kaufman, Y., and Nakajima, T.: AERONET—A federated instrument network and data
1146 archive for aerosol characterization, *Remote Sens. Environ.*, 66, 1-16,
1147 [https://doi.org/10.1016/S0034-4257\(98\)00031-5](https://doi.org/10.1016/S0034-4257(98)00031-5), 1998.
1148 Holben, B. N., Tanre, D., Smirnov, A., Eck, T., Slutsker, I., Abuhassan, N., Newcomb, W.,
1149 Schafer, J., Chatenet, B., and Lavenu, F.: An emerging ground-based aerosol climatology:
1150 Aerosol optical depth from AERONET, *J. Geophys. Res.- Atmos.*, 106, 12067-12097,
1151 <https://doi.org/10.1029/2001JD900014>, 2001.
1152 Hong, Y., and Di Girolamo, L.: Cloud phase characteristics over Southeast Asia from A-Train
1153 satellite observations, *Atmos. Chem. Phys.*, 20, 8267-8291, [https://doi.org/10.5194/acp-20-8267-](https://doi.org/10.5194/acp-20-8267-2020)
1154 2020, 2020.
1155 Hoppel, W., Frick, G., Fitzgerald, J., and Larson, R.: Marine boundary layer measurements of
1156 new particle formation and the effects nonprecipitating clouds have on aerosol size distribution,
1157 *J. Geophys. Res.- Atmos.*, 99, 14443-14459, <https://doi.org/10.1029/94JD00797>, 1994.
1158 Huang, C., Li, J., Sun, W., Chen, Q., Mao, Q.-J., and Yuan, Y.: Long-Term Variation
1159 Assessment of Aerosol Load and Dominant Types over Asia for Air Quality Studies Using
1160 Multi-Sources Aerosol Datasets, *Remote Sensing*, 13, 3116, <https://doi.org/10.3390/rs13163116>,
1161 2021.
1162 Hyer, E. J., Reid, J. S., Prins, E. M., Hoffman, J. P., Schmidt, C. C., Miettinen, J. I., and Giglio,
1163 L.: Patterns of fire activity over Indonesia and Malaysia from polar and geostationary satellite
1164 observations, *Atmos. Res.*, 122, 504-519, <https://doi.org/10.1016/j.atmosres.2012.06.011>, 2013.
1165 Jamora, J. B., Gudia, S. E. L., Go, A. W., Giduquio, M. B., and Loretero, M. E.: Potential CO2
1166 reduction and cost evaluation in use and transport of coal ash as cement replacement: A case in
1167 the Philippines, *Waste Manage.*, 103, 137-145, <https://doi.org/10.1016/j.wasman.2019.12.026>,
1168 2020.



- 1169 Jose, S., Gharai, B., Niranjana, K., and Rao, P.: Investigation on seasonal variations of aerosol
1170 properties and its influence on radiative effect over an urban location in central India, *Atmos.*
1171 *Environ.*, 133, 41-48, <https://doi.org/10.1016/j.atmosenv.2016.03.029>, 2016.
- 1172 Kaskaoutis, D., Kosmopoulos, P., Kambezidis, H., and Nastos, P.: Aerosol climatology and
1173 discrimination of different types over Athens, Greece, based on MODIS data, *Atmos. Environ.*,
1174 41, 7315-7329, <https://doi.org/10.1016/j.atmosenv.2007.05.017>, 2007.
- 1175 Kim, J.-S., and Park, K.: Atmospheric aging of Asian dust particles during long range transport,
1176 *Aerosol Sci. Tech.*, 46, 913-924, <https://doi.org/10.1080/02786826.2012.680984>, 2012.
- 1177 Kirchstetter, T. W., Novakov, T., and Hobbs, P. V.: Evidence that the spectral dependence of
1178 light absorption by aerosols is affected by organic carbon, *J. Geophys. Res.- Atmos.*, 109,
1179 <https://doi.org/10.1029/2004JD004999>, 2004.
- 1180 Koven, C. D., and Fung, I.: Inferring dust composition from wavelength-dependent absorption in
1181 Aerosol Robotic Network (AERONET) data, *J. Geophys. Res.- Atmos.*, 111,
1182 <https://doi.org/10.1029/2005JD006678>, 2006.
- 1183 Kudo, R., Nishizawa, T., and Aoyagi, T.: Vertical profiles of aerosol optical properties and the
1184 solar heating rate estimated by combining sky radiometer and lidar measurements, *Atmos. Meas.*
1185 *Tech.*, 9, 3223-3243, <https://doi.org/10.5194/amt-9-3223-2016>, 2016.
- 1186 Kumar, K. R., Sivakumar, V., Reddy, R. R., Gopal, K. R., and Adesina, A. J.: Identification and
1187 classification of different aerosol types over a subtropical rural site in Mpumalanga, South
1188 Africa: seasonal variations as retrieved from the AERONET Sunphotometer, *Aerosol Air Qual.*
1189 *Res.*, 14, 108-123, <https://doi.org/10.4209/aaqr.2013.03.0079>, 2014.
- 1190 Kumar, K. R., Yin, Y., Sivakumar, V., Kang, N., Yu, X., Diao, Y., Adesina, A. J., and Reddy,
1191 R.: Aerosol climatology and discrimination of aerosol types retrieved from MODIS, MISR and
1192 OMI over Durban (29.88 S, 31.02 E), South Africa, *Atmos. Environ.*, 117, 9-18,
1193 <https://doi.org/10.1016/j.atmosenv.2015.06.058>, 2015.
- 1194 Kuttippurath, J., and Raj, S.: Two decades of aerosol observations by AATSR, MISR, MODIS
1195 and MERRA-2 over India and Indian Ocean, *Remote Sens. Environ.*, 257, 112363,
1196 <https://doi.org/10.1016/j.rse.2021.112363>, 2021.
- 1197 Lee, H.-H., Iraqui, O., Gu, Y., Yim, S. H.-L., Chulakadabba, A., Tonks, A. Y.-M., Yang, Z., and
1198 Wang, C.: Impacts of air pollutants from fire and non-fire emissions on the regional air quality in
1199 Southeast Asia, *Atmos. Chem. Phys.*, 18, 6141-6156, <https://doi.org/10.5194/acp-18-6141-2018>,
1200 2018.
- 1201 Li, G., Bei, N., Cao, J., Huang, R., Wu, J., Feng, T., Wang, Y., Liu, S., Zhang, Q., and Tie, X.: A
1202 possible pathway for rapid growth of sulfate during haze days in China, *Atmos. Chem. Phys.*, 17,
1203 3301-3316, <https://doi.org/10.5194/acp-17-3301-2017>, 2017.
- 1204 Li, J., Carlson, B. E., and Laci, A. A.: Application of spectral analysis techniques in the
1205 intercomparison of aerosol data: 1. An EOF approach to analyze the spatial-temporal variability
1206 of aerosol optical depth using multiple remote sensing data sets, *J. Geophys. Res.- Atmos.*, 118,
1207 8640-8648, <https://doi.org/10.1002/jgrd.50686>, 2013.
- 1208 Li, Z., Niu, F., Fan, J., Liu, Y., Rosenfeld, D., and Ding, Y.: Long-term impacts of aerosols on
1209 the vertical development of clouds and precipitation, *Nat. Geosci.*, 4, 888-894,
1210 <https://doi.org/10.1038/ngeo1313>, 2011.
- 1211 Lin, N.-H., Sayer, A. M., Wang, S.-H., Loftus, A. M., Hsiao, T.-C., Sheu, G.-R., Hsu, N. C.,
1212 Tsay, S.-C., and Chantara, S.: Interactions between biomass-burning aerosols and clouds over
1213 Southeast Asia: Current status, challenges, and perspectives, *Environ. Pollut.*, 195, 292-307,
1214 <https://doi.org/10.1016/j.envpol.2014.06.036>, 2014.



- 1215 Lloyd, S.: Least squares quantization in PCM, *IEEE T. Inform. Theory*, 28, 129-137,
1216 <https://doi.org/10.1109/TIT.1982.1056489>, 1982.
- 1217 Lynch, P., Reid, J. S., Westphal, D. L., Zhang, J., Hogan, T. F., Hyer, E. J., Curtis, C. A., Hegg,
1218 D. A., Shi, Y., and Campbell, J. R.: An 11-year global gridded aerosol optical thickness
1219 reanalysis (v1. 0) for atmospheric and climate sciences, *Geosci. Model Dev.*, 9,
1220 <https://doi.org/10.5194/gmd-9-1489-2016>, 2016.
- 1221 Matsumoto, J., Olaguera, L. M. P., Nguyen-Le, D., Kubota, H., and Villafuerte, M. Q.:
1222 Climatological seasonal changes of wind and rainfall in the Philippines, *Int. J. Climatol.*, 40,
1223 4843-4857, <https://doi.org/10.1002/joc.6492>, 2020.
- 1224 Moosmüller, H., and Sorensen, C.: Small and large particle limits of single scattering albedo for
1225 homogeneous, spherical particles, *J. Quant. Spectrosc. Ra.*, 204, 250-255,
1226 <https://doi.org/10.1016/j.jqsrt.2017.09.029>, 2018.
- 1227 Mora, M., Braun, R. A., Shingler, T., and Sorooshian, A.: Analysis of remotely sensed and
1228 surface data of aerosols and meteorology for the Mexico Megalopolis Area between 2003 and
1229 2015, *J. Geophys. Res.- Atmos.*, 122, 8705-8723, <https://doi.org/10.1002/2017JD026739>, 2017.
- 1230 Nakata, M., Mukai, S., and Yasumoto, M.: Seasonal and regional characteristics of aerosol
1231 pollution in east and southeast Asia, *Frontiers in Environmental Science*, 6, 29, 2018.
- 1232 Fires and Smoke in Borneo: [https://earthobservatory.nasa.gov/images/40182/fires-and-smoke-in-](https://earthobservatory.nasa.gov/images/40182/fires-and-smoke-in-borneo)
1233 [borneo](https://earthobservatory.nasa.gov/images/40182/fires-and-smoke-in-borneo)), 2009.
- 1234 Nguyen, P., Shearer, E. J., Tran, H., Ombadi, M., Hayatbini, N., Palacios, T., Huynh, P.,
1235 Braithwaite, D., Updegraff, G., and Hsu, K.: The CHRS Data Portal, an easily accessible public
1236 repository for PERSIANN global satellite precipitation data, *Scientific Data*, 6, 1-10,
1237 <https://doi.org/10.1038/sdata.2018.296>, 2019.
- 1238 North, G. R., Bell, T. L., Cahalan, R. F., and Moeng, F. J.: Sampling errors in the estimation of
1239 empirical orthogonal functions, *Mon. Weather Rev.*, 110, 699-706, [https://doi.org/10.1175/1520-0493\(1982\)110<0699:SEITEO>2.0.CO;2](https://doi.org/10.1175/1520-0493(1982)110<0699:SEITEO>2.0.CO;2), 1982.
- 1241 O'Neill, N., Eck, T., Smirnov, A., Holben, B., and Thulasiraman, S.: Spectral discrimination of
1242 coarse and fine mode optical depth, *J. Geophys. Res.- Atmos.*, 108,
1243 <https://doi.org/10.1029/2002JD002975>, 2003.
- 1244 Oanh, N. T. K., Permadi, D. A., Hopke, P. K., Smith, K. R., Dong, N. P., and Dang, A. N.:
1245 Annual emissions of air toxics emitted from crop residue open burning in Southeast Asia over
1246 the period of 2010–2015, *Atmos. Environ.*, 187, 163-173,
1247 <https://doi.org/10.1016/j.atmosenv.2018.05.061>, 2018.
- 1248 Pace, G., Sarra, A. d., Meloni, D., Piacentino, S., and Chamard, P.: Aerosol optical properties at
1249 Lampedusa (Central Mediterranean). 1. Influence of transport and identification of different
1250 aerosol types, *Atmos. Chem. Phys.*, 6, 697-713, <https://doi.org/10.5194/acp-6-697-2006>, 2006.
- 1251 Pandolfi, M., Alados-Arboledas, L., Alastuey, A., Andrade, M., Angelov, C., Artiñano, B.,
1252 Backman, J., Baltensperger, U., Bonasoni, P., and Bukowiecki, N.: A European aerosol
1253 phenomenology–6: scattering properties of atmospheric aerosol particles from 28 ACTRIS sites,
1254 *Atmos. Chem. Phys.*, 18, 7877-7911, <https://doi.org/10.5194/acp-18-7877-2018>, 2018.
- 1255 Petters, M. D., Carrico, C. M., Kreidenweis, S. M., Prenni, A. J., DeMott, P. J., Collett Jr, J. L.,
1256 and Moosmüller, H.: Cloud condensation nucleation activity of biomass burning aerosol, *J.*
1257 *Geophys. Res.- Atmos.*, 114, <https://doi.org/10.1029/2009JD012353>, 2009.
- 1258 Plymale, N. T., Szekely, J. E., and Rubinstein, A. H.: Statistical Cluster Analysis of Global
1259 Aerosol Optical Depth for Simplified Atmospheric Modeling, *J. Appl. Meteorol. Clim.*,
1260 <https://doi.org/10.1175/JAMC-D-21-0150.1>, 2021.



- 1261 PSA: Highlights of the Philippine population 2015 census of population, Philippine Statistics
1262 Authority, 2016.
- 1263 Randles, C., Da Silva, A., Buchard, V., Colarco, P., Darmenov, A., Govindaraju, R., Smirnov,
1264 A., Holben, B., Ferrare, R., and Hair, J.: The MERRA-2 aerosol reanalysis, 1980 onward. Part I:
1265 System description and data assimilation evaluation, *J. Climate*, 30, 6823–6850,
1266 <https://doi.org/10.1175/JCLI-D-16-0609.1>, 2017.
- 1267 Reid, J., Koppmann, R., Eck, T., and Eleuterio, D.: A review of biomass burning emissions part
1268 II: intensive physical properties of biomass burning particles, *Atmos. Chem. Phys.*, 5, 799–825,
1269 <https://doi.org/10.5194/acp-5-799-2005>, 2005.
- 1270 Reid, J., Xian, P., Hyer, E., Flatau, M., Ramirez, E., Turk, F., Sampson, C., Zhang, C., Fukada,
1271 E., and Maloney, E.: Multi-scale meteorological conceptual analysis of observed active fire
1272 hotspot activity and smoke optical depth in the Maritime Continent, *Atmos. Chem. Phys.*, 12,
1273 2117, <https://doi.org/10.5194/acp-12-2117-2012>, 2012.
- 1274 Reid, J., Maring, H., Narisma, G., van den Heever, S., Di Girolamo, L., Ferrare, R., Holz, R.,
1275 Lawson, P., Mace, G., and Simpas, J.: The coupling between tropical meteorology, aerosol
1276 lifecycle, convection, and radiation, during the Cloud, Aerosol and Monsoon Processes
1277 Philippines Experiment (CAMP 2 Ex), *B. Am. Meteorol. Soc.*, [https://doi.org/10.1175/BAMS-](https://doi.org/10.1175/BAMS-D-21-0285.1)
1278 [D-21-0285.1](https://doi.org/10.1175/BAMS-D-21-0285.1), 2023.
- 1279 Reid, J. S., Hobbs, P. V., Liousse, C., Martins, J. V., Weiss, R. E., and Eck, T. F.: Comparisons
1280 of techniques for measuring shortwave absorption and black carbon content of aerosols from
1281 biomass burning in Brazil, *J. Geophys. Res.- Atmos.*, 103, 32031–32040,
1282 <https://doi.org/10.1029/98JD00773>, 1998.
- 1283 Reid, J. S., Hyer, E. J., Johnson, R. S., Holben, B. N., Yokelson, R. J., Zhang, J., Campbell, J. R.,
1284 Christopher, S. A., Di Girolamo, L., and Giglio, L.: Observing and understanding the Southeast
1285 Asian aerosol system by remote sensing: An initial review and analysis for the Seven Southeast
1286 Asian Studies (7SEAS) program, *Atmos. Res.*, 122, 403–468,
1287 <https://doi.org/10.1016/j.atmosres.2012.06.005>, 2013.
- 1288 Reid, J. S., Lagrosas, N. D., Jonsson, H. H., Reid, E. A., Sessions, W. R., Simpas, J. B., Uy, S.
1289 N., Boyd, T., Atwood, S. A., and Blake, D. R.: Observations of the temporal variability in
1290 aerosol properties and their relationships to meteorology in the summer monsoonal South China
1291 Sea/East Sea: the scale-dependent role of monsoonal flows, the Madden–Julian Oscillation,
1292 tropical cyclones, squall lines and cold pools, *Atmos. Chem. Phys.*, 15, 1745–1768,
1293 <https://doi.org/10.5194/acp-15-1745-2015>, 2015.
- 1294 Rolph, G., Stein, A., and Stunder, B.: Real-time environmental applications and display system:
1295 READY, *Environ. Modell. Softw.*, 95, 210–228, <https://doi.org/10.1016/j.envsoft.2017.06.025>,
1296 2017.
- 1297 Ross, J. L., Hobbs, P. V., and Holben, B.: Radiative characteristics of regional hazes dominated
1298 by smoke from biomass burning in Brazil: Closure tests and direct radiative forcing, *J. Geophys.*
1299 *Res.- Atmos.*, 103, 31925–31941, <https://doi.org/10.1029/97JD03677>, 1998.
- 1300 Saleh, R., Hennigan, C., McMeeking, G., Chuang, W., Robinson, E., Coe, H., Donahue, N., and
1301 Robinson, A.: Absorptivity of brown carbon in fresh and photo-chemically aged biomass-
1302 burning emissions, *Atmos. Chem. Phys.*, 13, 7683–7693, [https://doi.org/10.5194/acp-13-7683-](https://doi.org/10.5194/acp-13-7683-2013)
1303 [2013](https://doi.org/10.5194/acp-13-7683-2013), 2013.
- 1304 Schlosser, J. S., Braun, R. A., Bradley, T., Dadashazar, H., MacDonald, A. B., Aldhaif, A. A.,
1305 Aghdam, M. A., Mardi, A. H., Xian, P., and Sorooshian, A.: Analysis of aerosol composition
1306 data for western United States wildfires between 2005 and 2015: Dust emissions, chloride



- 1307 depletion, and most enhanced aerosol constituents, *J. Geophys. Res.- Atmos.*, 122, 8951-8966,
1308 <https://doi.org/10.1002/2017JD026547>, 2017.
- 1309 Schuster, G., Dubovik, O., and Arola, A.: Remote sensing of soot carbon–Part 1: Distinguishing
1310 different absorbing aerosol species, *Atmos. Chem. Phys.*, 16, 1565-1585,
1311 <https://doi.org/10.5194/acp-16-1565-2016>, 2016.
- 1312 Schuster, G. L., Dubovik, O., Holben, B. N., and Clothiaux, E. E.: Inferring black carbon content
1313 and specific absorption from Aerosol Robotic Network (AERONET) aerosol retrievals, *J.*
1314 *Geophys. Res.- Atmos.*, 110, <https://doi.org/10.1029/2004JD004548>, 2005.
- 1315 Schuster, G. L., Dubovik, O., and Holben, B. N.: Angstrom exponent and bimodal aerosol size
1316 distributions, *J. Geophys. Res.- Atmos.*, 111, <https://doi.org/10.1029/2005JD006328>, 2006.
- 1317 Sharma, M., Kaskaoutis, D. G., Singh, R. P., and Singh, S.: Seasonal variability of atmospheric
1318 aerosol parameters over Greater Noida using ground sunphotometer observations, *Aerosol Air*
1319 *Qual. Res.*, 14, 608-622, <https://doi.org/10.4209/aaqr.2013.06.0219>, 2014.
- 1320 Shen, Z., Liu, J., Horowitz, L., Henze, D., Fan, S., Mauzerall, D. L., Lin, J.-T., and Tao, S.:
1321 Analysis of transpacific transport of black carbon during HIPPO-3: implications for black carbon
1322 aging, *Atmos. Chem. Phys.*, 14, 6315-6327, <https://doi.org/10.5194/acp-14-6315-2014>, 2014.
- 1323 Smirnov, A., Holben, B. N., Dubovik, O., O'Neill, N. T., Eck, T. F., Westphal, D. L., Goroch, A.
1324 K., Pietras, C., and Slutsker, I.: Atmospheric aerosol optical properties in the Persian Gulf, *J.*
1325 *Atmos. Sci.*, 59, 620-634, [https://doi.org/10.1175/1520-0469\(2002\)059<0620:AAOPIT>2.0.CO;2](https://doi.org/10.1175/1520-0469(2002)059<0620:AAOPIT>2.0.CO;2), 2002.
- 1327 Smith, S. J., Aardenne, J. v., Klimont, Z., Andres, R. J., Volke, A., and Delgado Arias, S.:
1328 Anthropogenic sulfur dioxide emissions: 1850–2005, *Atmos. Chem. Phys.*, 11, 1101-1116,
1329 <https://doi.org/10.5194/acp-11-1101-2011>, 2011.
- 1330 Sorooshian, A., Wang, Z., Feingold, G., and L'Ecuyer, T. S.: A satellite perspective on cloud
1331 water to rain water conversion rates and relationships with environmental conditions, *J.*
1332 *Geophys. Res.- Atmos.*, 118, 6643-6650, <https://doi.org/10.1002/jgrd.50523>, 2013.
- 1333 Stahl, C., Cruz, M. T., Bañaga, P. A., Betito, G., Braun, R. A., Aghdam, M. A., Cambaliza, M.
1334 O., Lorenzo, G. R., MacDonald, A. B., and Hilario, M. R. A.: Sources and characteristics of size-
1335 resolved particulate organic acids and methanesulfonate in a coastal megacity: Manila,
1336 Philippines, *Atmos. Chem. Phys.*, 20, 15907-15935, <https://doi.org/10.5194/acp-20-15907-2020>,
1337 2020.
- 1338 Stahl, C., Crosbie, E., Bañaga, P. A., Betito, G., Braun, R. A., Cainglet, Z. M., Cambaliza, M. O.,
1339 Cruz, M. T., Dado, J. M., and Hilario, M. R. A.: Total organic carbon and the contribution from
1340 speciated organics in cloud water: airborne data analysis from the CAMP 2 Ex field campaign,
1341 *Atmos. Chem. Phys.*, 21, 14109-14129, <https://doi.org/10.5194/acp-21-14109-2021>, 2021.
- 1342 Stein, A., Draxler, R. R., Rolph, G. D., Stunder, B. J., Cohen, M., and Ngan, F.: NOAA's
1343 HYSPLIT atmospheric transport and dispersion modeling system, *B. Am. Meteorol. Soc.*, 96,
1344 2059-2077, <https://doi.org/10.1175/BAMS-D-14-00110.1>, 2015.
- 1345 Stevens, B., and Feingold, G.: Untangling aerosol effects on clouds and precipitation in a
1346 buffered system, *Nature*, 461, 607-613, <https://doi.org/10.1038/nature08281>, 2009.
- 1347 Sullivan, R. C., Levy, R. C., da Silva, A. M., and Pryor, S. C.: Developing and diagnosing
1348 climate change indicators of regional aerosol optical properties, *Scientific Reports*, 7, 1-13,
1349 <https://doi.org/10.1038/s41598-017-18402-x>, 2017.
- 1350 Tao, W. K., Chen, J. P., Li, Z., Wang, C., and Zhang, C.: Impact of aerosols on convective
1351 clouds and precipitation, *Rev. Geophys.*, 50, <https://doi.org/10.1029/2011RG000369>, 2012.



- 1352 Tsay, S.-C., Hsu, N. C., Lau, W. K.-M., Li, C., Gabriel, P. M., Ji, Q., Holben, B. N., Welton, E.
1353 J., Nguyen, A. X., and Janjai, S.: From BASE-ASIA toward 7-SEAS: A satellite-surface
1354 perspective of boreal spring biomass-burning aerosols and clouds in Southeast Asia,
1355 *Atmospheric environment*, 78, 20-34, 2013.
- 1356 Van Beelen, A., Roelofs, G., Hasekamp, O., Henzing, J., and Röckmann, T.: Estimation of
1357 aerosol water and chemical composition from AERONET Sun-sky radiometer measurements at
1358 Cabauw, the Netherlands, *Atmos. Chem. Phys.*, 14, 5969-5987, [https://doi.org/10.5194/acp-14-](https://doi.org/10.5194/acp-14-5969-2014)
1359 [5969-2014](https://doi.org/10.5194/acp-14-5969-2014), 2014.
- 1360 Wang, L., Lau, K.-H., Fung, C.-H., and Gan, J.-P.: The relative vorticity of ocean surface winds
1361 from the QuikSCAT satellite and its effects on the geneses of tropical cyclones in the South
1362 China Sea, *Tellus A*, 59, 562-569, <https://doi.org/10.1111/j.1600-0870.2007.00249.x>, 2007.
- 1363 Wu, M.-c., and Choy, C.-w.: An Observational Study of the Changes in the Intensity and Motion
1364 of Tropical Cyclones crossing Luzon, *Tropical Cyclone Research and Review*, 4, 95-109,
1365 <https://doi.org/10.6057/2015TCRRh3.01>, 2016.
- 1366 Xian, P., Reid, J. S., Atwood, S. A., Johnson, R. S., Hyer, E. J., Westphal, D. L., and Sessions,
1367 W.: Smoke aerosol transport patterns over the Maritime Continent, *Atmos. Res.*, 122, 469-485,
1368 <https://doi.org/10.1016/j.atmosres.2012.05.006>, 2013.
- 1369 Xie, Y., Li, Z., Zhang, Y., Zhang, Y., Li, D., Li, K., Xu, H., Zhang, Y., Wang, Y., and Chen, X.:
1370 Estimation of atmospheric aerosol composition from ground-based remote sensing
1371 measurements of Sun-sky radiometer, *J. Geophys. Res.- Atmos.*, 122, 498-518,
1372 <https://doi.org/10.1002/2016JD025839>, 2017.
- 1373 Zhao, G., Zhao, C., Kuang, Y., Bian, Y., Tao, J., Shen, C., and Yu, Y.: Calculating the aerosol
1374 asymmetry factor based on measurements from the humidified nephelometer system, *Atmos.*
1375 *Chem. Phys.*, 18, 9049-9060, <https://doi.org/10.5194/acp-18-9049-2018>, 2018.